ELECTROCHEMICAL ANALYSIS OF VANADIUM DOPED ZINC SULFIDE

by
BERFU AKGÜL

Submitted to the Graduate School of Engineering and Natural Sciences
in partial fulfilment of
the requirements for the degree of Master of Science

Sabancı University
July 2025

ELECTROCHEMICAL ANALYSIS OF VANADIUM DOPED ZINC SULFIDE

Approved by:

Prof. EMRE ERDEM .....
(Thesis Supervisor)

Assoc. Prof. FERAY BAKAN MISIRLIOĞLU .....

Assoc. Prof. HÜLYA BİÇER .....

Date of Approval: July 21, 2025

ABSTRACT

ELECTROCHEMICAL ANALYSIS OF VANADIUM DOPED ZINC SULFIDE

BERFU AKGÜL

Materials Science and Nano Engineering M.Sc. Thesis, July 2025

Thesis Supervisor: Prof. Emre Erdem

Keywords: Cyclic voltammetry, defect engineering, supercapacitor, vanadium doping, zinc sulfide

This thesis investigates the structural, optical, and electrochemical properties of vanadium-doped zinc sulfide (ZnS:V) nanoparticles synthesized via precipitation synthesis for application as electrode materials in supercapacitors. ZnS, a wide bandgap semiconductor with limited intrinsic conductivity and capacitance, was doped with varying concentrations of vanadium (0.3–1%) to enhance its electrochemical performance. X-ray diffraction (XRD) analysis confirmed the cubic sphalerite structure with slight lattice distortions induced by vanadium incorporation, while UV–Vis spectroscopy revealed band gap modulation due to sp–d exchange interactions and the Burstein–Moss effect. Scanning transmission electron microscopy (STEM) demonstrated well-dispersed nanoparticles with spherical morphology, and electron paramagnetic resonance (EPR) spectroscopy detected characteristic signals indicating successful doping and defect formation. Photoluminescence (PL) analysis showed defect-related emissions, supporting the presence of intrinsic and dopant-induced states influencing carrier recombination. Electrochemical characterization was performed using cyclic voltammetry (CV), potentiostatic electrochemical impedance spectroscopy (PEIS), and galvanostatic charge–discharge (GCPL) techniques. CV and Dunn analysis revealed a substantial increase in both capacitive and diffusive contributions upon vanadium doping, attributed to enhanced redox activity and improved ion diffusion. PEIS results demonstrated a marked reduction in charge-transfer resistance and Warburg impedance in doped samples, indicating improved electronic conductivity and facile ion transport. Overall, vanadium doping significantly enhanced the specific capacitance, rate capability, and charge storage mechanisms of ZnS electrodes. This study highlights the potential of defect engi-

neering and vanadium doping as effective strategies to enhance the electrochemical performance of ZnS-based electrodes for high-performance supercapacitor applications.

ÖZET

VANADYUM KATKILI ÇİNKO SÜLFÜRÜN ELEKTROKİMYASAL ANALİZİ

BERFU AKGÜL

Malzeme Bilimi ve Nano Mühendislik Yüksek Lisans Tezi, Temmuz 2025

Tez Danışmanı: Prof. Dr. Emre Erdem

Anahtar Kelimeler: Çevrimsel voltametri, kusur mühendisliği, süperkapasitör, vanadyum katkılama, çinko sülfür

Bu tez, süperkapasitörlerde elektrot malzemesi olarak kullanılmak üzere çökelme yöntemiyle sentezlenen vanadyum katkılı çinko sülfür (ZnS:V) nanoparçacıklarının yapısal, optik ve elektrokimyasal özelliklerini araştırmaktadır. Geniş bant aralığına sahip, sınırlı elektriksel iletkenlik ve kapasitansa sahip bir yarıiletken olan ZnS'nin elektrokimyasal performansını artırmak amacıyla %0.3–1 oranlarında vanadyum ile katkılanmıştır. X-ışını kırınımı (XRD) analizi, vanadyum katkılanması sonucu oluşan hafif örgü bozulmalarıyla birlikte kübik sfalerit yapısını doğrulamıştır. UV–Vis spektroskopisi ise sp–d değişim etkileşimleri ve Burstein–Moss etkisi nedeniyle bant aralığında modülasyon olduğunu ortaya koymuştur. Tarama geçirimli elektron mikroskobu (STEM) analizleri, küresel morfolojiye sahip, iyi dağılmış nanoparçacıklar göstermiştir. Elektron paramanyetik rezonans (EPR) spektroskopisi ise başarılı katkılama ve kusur oluşumunu gösteren karakteristik sinyalleri tespit etmiştir. Fotolüminesans (PL) analizi, taşıyıcı yeniden birleşimini etkileyen içsel ve katkı kaynaklı durumların varlığını destekleyen kusur ilişkili emisyonlar göstermiştir. Elektrokimyasal karakterizasyon; çevrimsel voltametri (CV), potansiyostatik elektrokimyasal empedans spektroskopisi (PEIS) ve galvanostatik şarj–deşarj (GCPL) teknikleri kullanılarak gerçekleştirilmiştir. CV ve Dunn analizi, vanadyum katkılamasıyla birlikte kapasitif ve difüzif katkılarda önemli bir artış olduğunu ve bunun, artan redoks aktivitesi ile iyileşen iyon difüzyonuna atfedildiğini göstermiştir. PEIS sonuçları, katkılı örneklerde yük transfer direncinde ve Warburg empedansında belirgin bir azalma olduğunu, bunun da gelişmiş elektriksel iletkenlik ve kolay iyon taşınımına işaret ettiğini ortaya koymuştur. Genel olarak, vanadyum katkılama, ZnS elektrotlarının özgül kapasitansını, hız kabiliyetini ve yük depolama

mekanizmalarını önemli ölçüde iyileştirmiştir. Bu çalışma, ZnS tabanlı elektrotların elektrokimyasal performansını artırmak için kusur mühendisliği ve vanadyum katkılamanın etkili stratejiler olarak potansiyelini vurgulamaktadır.

ACKNOWLEDGEMENTS

This journey has been at times challenging and at times full of joy. I am deeply grateful to my advisor, Prof. Emre Erdem, for his invaluable assistance and unwavering support. I would also like to sincerely thank Prof. Mehmet Ali Gülgün, who has played a significant role in shaping the person I am today. Additionally, I extend my sincere gratitude to Prof. Mehmet Kesim, who has never withheld his understanding and support throughout this pursuit of seeking what knowledge truly means through self-understanding.

My heartfelt thanks go to my generous lab mate Hasan, who has always been there when I needed help and has contributed immensely to my work. I also extend my profound thanks to Dr. Arpad Mihai Rostas, Dr. Ahmet Güngör, Bilge Esenkal, and my lab mate Deniz for their valuable support and contributions throughout this process. I warmly thank all my professors who, since my undergraduate years, have broadened my perspective and helped me embrace the true spirit of learning.

To my dearest friends Esra, Ali, and Mervenaz, thank you for being there through every laugh and every sorrow. You were a breath of fresh air during my most difficult moments, and I'm so grateful for our bond.

Most of all, I owe infinite thanks to my family. I thank my mother, who lifted me up when I fell, never withheld her compassion, and never stopped believing in me. I thank my father, who always supported me. And my brother, Ersagun, having a brother like you is one of the greatest blessings in my life. On this journey where we are both together and alone, thank you for being that calm harbor where I can find rest. I am grateful for everything you have done for me and the vision you've added to my life. And Güzin, I consider myself incredibly fortunate to have you as the kind and generous sister I have always longed for since childhood, someone in whom I can place trust and with whom I can share everything. You hold an irreplaceable and a special place in my heart.

Finally, to my husband, my companion, and my best friend, Ege, everything in life has meaning when I get to share it with you. Thank you for opening your beautiful heart to me and for always being by my side. Having you in my life is a true blessing.

To Ankara

TABLE OF CONTENTS

LIST OF TABLES

LIST OF FIGURES

LIST OF ABBREVIATIONS

ZnS	zinc sulfide
CVD	Chemical Vapor Deposition
ZnS:V	vanadium-doped zinc sulfide
EPR	Electron Paramagnetic Resonance
PL	Photoluminescence
XRD	X-ray Diffraction
STEM	Scanning Transmission Electron Microscopy
CV	Cyclic Voltammetry
PEIS	Potentiostatic Electrochemical Impedance Spectroscopy
GCPL	Galvanostatic Charge–Discharge with Potential Limitation
$\beta - ZnS$	cubic sphalerite
TM	transition-metal
DD	double-distilled
PVP	polyvinylpyrrolidone
TAA	thioacetamide
FWHM	full width at half maximum
UV-Vis	ultraviolet–visible
CW	continuous-wave
VH	voltage holding
SC	supercapacitor
ESR	equivalent series resistance
E_d	energy density
P_d	power density
Δt	discharge time
EDLC	electric double-layer capacitor
GO	graphene oxide
$NaVO_3$	Sodium metavanadate

1. INTRODUCTION

The accelerating need to reduce reliance on fossil fuels and to support the stable integration of intermittent renewable sources has made large-scale electrical energy storage systems more crucial than ever (J. Liu et al., 2013). Supercapacitors, particularly those employing electrochemical mechanisms, have garnered increasing attention as viable solutions (Dissanayake & Kularatna-Abeywardana, 2024). Their fast charging and discharging behavior, long operational lifespan, and structural reliability make them well-suited for modern energy infrastructure (Mehra, Saxena, & Bhullar, 2024). However, the efficiency and long-term viability of these devices are fundamentally tied to the electrode materials used, which directly impact their energy and power densities (Ahmed et al., 2024).

Among the variants of electrochemical storage devices, supercapacitors have emerged as particularly promising candidates due to their enhanced power densities, fast charge kinetics, and extended cycle stability (Yadlapalli, Alla, Kandipati, & Kotapati, 2022). These advantages hinge largely on the performance of the electrode materials involved, making their selection and engineering a pivotal aspect of device design (Forouzandeh, Kumaravel, & Pillai, 2020). The choice of materials determines not only the charge storage mechanism but also the overall electrochemical stability and responsiveness of the system. As a result, optimizing electrode material is essential for improving device performance (Alam et al., 2024).

Zinc sulfide (ZnS), a transition metal sulfide, has attracted attention due to its semiconducting nature (D'Amico et al., 2017), promising theoretical capacitance (Yi, Li, Li, Luo, & Liu, 2019), and environmentally benign composition (Xiao et al., 2012). It is regarded as a promising unconventional material for use in photoluminescent (Xiao et al., 2012), electroluminescent (Wright & Viney, 2001), and cathodoluminescent (H. Liu et al., 2013) applications, owing to its enhanced chemical stability relative to other chalcogenides like ZnSe (Rathore et al., 2008). Yet the electrochemical characteristics of ZnS in its nanostructured form differ significantly from those in the bulk phase (Mane et al., 2024). Nanostructured semiconductors exhibit electrical and optical properties that lie between those of large crystalline solids and

molecular systems (Ganguly, Halder, Haque, Das, & Dastidar, 2015). These differences arise primarily from quantum confinement effects and the high proportion of surface atoms, both of which profoundly influence electron transport and surface reactivity (Ganguly et al., 2015). Such unique properties have stimulated intensive research into the synthesis of ZnS and similar compounds using wet-chemical techniques to better harness their nanoscale behavior (Mane et al., 2024).

To fully leverage these nanostructure-induced benefits, parameters like specific capacitance, surface area, ion diffusion, and conductivity must be meticulously optimized (Shrivastav et al., 2021). These characteristics determine how efficiently a supercapacitor stores and delivers charge. One of the most successful strategies for enhancing these parameters is doping (Shrivastav et al., 2021), altering electronic configurations (Forouzandeh et al., 2020), and create additional active sites (Forouzandeh et al., 2020). Doping not only improves conductivity but also adjusts the energy band structure and enhances electrochemical reactivity (Maswanganye, Kabongo, & Dhlamini, 2022). Therefore, vanadium is selected as a dopant for ZnS due to its ability to introduce a high density of surface defects and active sites that enhance ion adsorption and redox reactivity (Rana, Das, Rahman, Ahmed, & Hossain, 2021). Its multiple oxidation states (V^{+3}/V^{+4}) enable fast and reversible Faradaic reactions, contributing significantly to pseudocapacitive charge storage. In addition, vanadium improves the electrical conductivity of ZnS, facilitating efficient electron transport and enhancing the overall electrochemical performance (Rana et al., 2021). Various synthesis methods have been employed to fabricate ZnS nanoma-

Table 1.1 Different types of synthesis techniques of ZnS and their comparison.

Synthesis Method	**Key Features**	**Doping Precision**	**Scalability**
Hydrothermal	Good crystallinity, morphology control	Moderate	High
Sonochemical	Rapid synthesis, nanoparticle dispersion	Moderate	Moderate
Co-precipitation	Simple, cost-effective	Moderate	High
Chemical Vapor Deposition	High film purity and uniform thickness	High	Low
Magnetron Sputtering	Precise doping, excellent thin-film control	Very High	Moderate

terials. As you can see from Table 1.1 techniques like hydrothermal (Shah, Sajjad, Hou, BiBi, & Shah, 2022), sonochemical (G.-J. Lee, Anandan, Masten, & Wu, 2014), chemical vapor deposition (CVD) (El Khouja et al., 2024), co-precipitation (Tom et al., 2025), and magnetron sputtering (Haque et al., 2014) offer different degrees of control over particle size, crystallinity, and doping uniformity (Alam et al., 2024).

By strategically combining precursor selection, nanostructuring, doping, and advanced synthesis routes it becomes possible to systematically enhance the electrochemical performance of ZnS-based supercapacitors (Ahmed et al., 2024), contributing to a new generation of efficient, scalable, and durable energy storage systems.

This thesis is structured to comprehensively explore the synthesis, characterization, and electrochemical evaluation of vanadium-doped zinc sulfide (ZnS:V) as a potential electrode material. Each chapter is designed to build a logical progression from fundamental concepts to experimental outcomes. In this chapter, we have detailed the rationale behind using ZnS as an electrode material, highlighted the role of nanostructuring and vanadium doping, and compared various synthesis methods to demonstrate strategies for enhancing its electrochemical performance in supercapacitor applications. Chapter 2 introduces the physical and chemical properties of ZnS, highlighting its semiconducting behavior, structural characteristics, and potential suitability for energy storage applications. This foundational understanding is essential for appreciating the significance of subsequent modifications and analyses. Following the discussion of ZnS properties, Chapter 3 provides a concise overview of two key spectroscopic techniques: electron paramagnetic resonance (EPR) and photoluminescence (PL) spectroscopy. These methods are crucial for identifying and interpreting defect states and electronic transitions in semiconducting materials. The underlying principles of each technique will be outlined.

The methodology is presented in Chapter 4 details the synthesis procedures for both undoped and vanadium-doped ZnS, with particular attention to the chemical precursors, reaction conditions, and processing parameters. Each subsequent section will describe the technical parameters of the characterization methods employed, including X-ray diffraction (XRD) for crystallographic analysis, scanning transmission electron microscopy (STEM) for morphological examination, and EPR and PL for probing the nature and density of defect states. Additionally, this chapter includes a section outlining the design of the supercapacitor configuration used for electrochemical testing, including information on cell assembly and electrolyte selection. The operational parameters for cyclic voltammetry (CV), potentiostatic electrochemical impedance spectroscopy (PEIS), and galvanostatic charge–discharge with potential limitation (GCPL) techniques are included to ensure reproducibility and

interpretability of the electrochemical data.

In Chapter 5, the results and discussion section will integrate the structural, morphological, and spectroscopic findings with the electrochemical performance of ZnS:V electrodes. Emphasis will be placed on correlating the observed changes due to defect structure revealed by XRD, SEM, EPR, and PL with improvements or variations in electrochemical behavior. In particular, the electrochemical performance metrics obtained from CV, GCPL, and EIS will be analyzed in terms of specific capacitance, rate capability, and charge-transfer resistance.

This thesis undertakes a systematic investigation into the electrochemical energy storage behavior of ZnS modified through vanadium doping. It aims to elucidate the rationale behind V incorporation and its influence on the structural, electronic, and electrochemical properties of ZnS. By leveraging defect engineering as a tool, the study seeks to modulate the material's band structure, increase active surface sites, and enhance charge storage properties. The resulting effects on supercapacitive performance will be critically evaluated through an analysis of structural characterization, spectroscopic profiling, and electrochemical measurements, providing a comprehensive framework for the design of ZnS as an advanced electrode material.

2. PROPERTIES OF ZnS

Zinc sulfide (ZnS) is a wide bandgap semiconductor belonging to the II–VI group, recognized for its structural stability and tunable morphology (Dong et al., 2022; Yi et al., 2019). It exists in two main crystalline phases, most stable cubic sphalerite (β-ZnS) shown in Fig 2.1 and hexagonal wurtzite, each exhibiting distinct band gap values, with the cubic form being especially notable for ultraviolet optoelectronic applications due to its large band gap of approximately 3.7 eV at room temperature (Adachi, 1999). The electronic band structure of ZnS nanoparticles is highly sensitive to surface defects, and adjusting the particle size distribution is essential to modulate the band gap, which directly influences their capacitance performance (Jubeer et al., 2023). Despite its potential, pristine ZnS and its composite electrodes generally exhibit low specific capacitance and unsatisfactory rate capability (Saleem, Khalid, Malik, & Nazir, 2024). To address these limitations, this study employs vanadium doping to enhance the electrochemical storage characteristics of cubic sphalerite ZnS, aiming to produce more efficient electrode materials for supercapacitor applications.

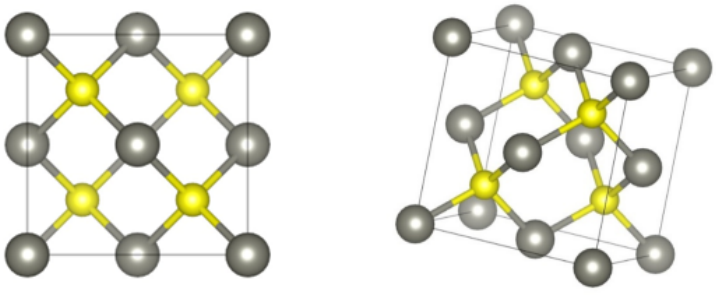

Figure 2.1 ZnS cubic sphalerite (β-ZnS) crystal structure (yellow Zn^{+2} – grey S^{-2}).

A range of ZnS-based nanoscale architectures such as nanowires (Li et al., 2019), nanotubes (An, Meng, Xiong, & Qiu, 2017), and nanoribbons (Kar & Chaudhuri, 2005) have been effectively produced and are well-suited for incorporation into nanoscale electronic systems. Notably, hybrid structures and multilayers combining ZnS with

its counterpart ZnO have attracted significant interest due to their potential in applications like piezotronic devices, solar energy conversion, and light detection technologies (D'Amico et al., 2017).

Table 2.1 Physical properties of ZnS.

Property	**Value**
Crystal structure	Cubic sphalerite (β-ZnS)
Lattice constant	5.4102 Å
Melting point	1827 °C
Density	4.0879 g/cm^3
Bandgap energy E_g	3.7 eV at room temperature
The effective mass of electrons	0.24 m_0
The effective mass of holes	0.28 m_0
Refractive index	2.356
Exciton binding energy	39 meV
Dielectric constant	8.9

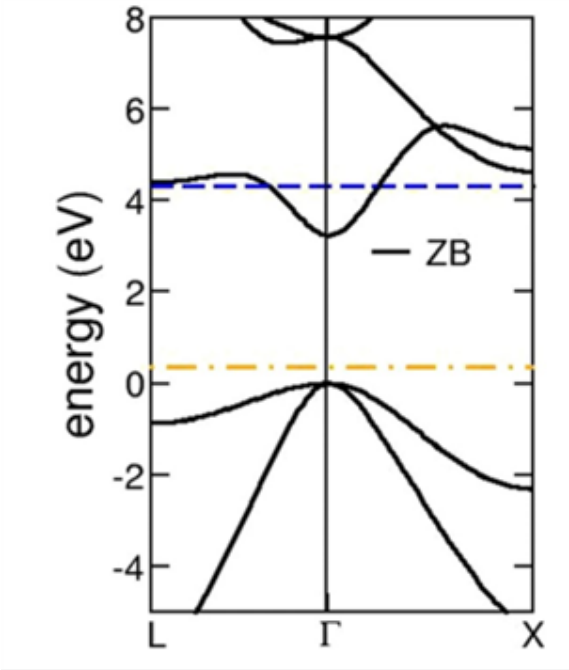

Figure 2.2 Band structure of ZnS for cubic sphalerite crystal structure(D'Amico et al., 2017).

As D'Amico *et al.* demonstrate, as it is shown in Fig 2.2, in the cubic sphalerite phase of ZnS, the conduction band exhibits a single well-defined energy branch extending throughout the Brillouin zone, characterized by an approximately parabolic dispersion near the Γ point (D'Amico et al., 2017). This band curvature indicates a low effective mass for conduction electrons and reflects nearly free-electron-like

behavior within the crystal potential. Upon n-type doping, excess electrons occupy this parabolic conduction band minimum resulting in a quasi-free electron gas with high carrier mobility and delocalized transport characteristics (D'Amico et al., 2017). This feature is critical for enabling efficient electrical conduction via high mobility in doped ZnS systems.

3. INTRODUCTION TO ELECTRON PARAMAGNETIC RESONANCE (EPR) SPECTROSCOPY AND PHOTOLUMINESCENCE (PL) SPECTROSCOPY

3.1 Electron Paramagnetic Resonance (EPR) Spectroscopy

The following is a concise summary of electron paramagnetic resonance (EPR) theory, based on the chapter titled *EPR Spectroscopy: Theory* authored by Christopher C. Rowlands and Damien M. Murphy (Lindon, Tranter, & Koppenaal, 2016).

EPR is a magnetic resonance method that probes unpaired electrons in a material. In an applied static field B_0, an electron which has an intrinsic spin quantum number $S = \frac{1}{2}$, can occupy two spin states, one aligned with the field and one against it, and each electron (magnetic moment $\mu = g\mu_B B_0$) has two Zeeman levels separated by an energy:

$$\Delta E = g_e \mu_B B_0 \tag{3.1}$$

where μ_B is Bohr magneton and $g_e \approx 2.0023$ for a free electron. When microwave radiation of frequency ν is applied, resonance occurs when:

$$h\nu = \Delta E \tag{3.2}$$

This yields the fundamental EPR condition:

$$h\nu = g_e \mu_B B_0 \tag{3.3}$$

where h is Planck's constant. In practice X-band microwaves (∼9-10 GHz) are often used, so typical resonance fields are a few tenths of a tesla. The measured EPR signal (usually the first derivative of the absorption) directly reports on g and thus on the local electronic environment. In defects or transition-metal dopants, crystal fields and spin-orbit coupling shift the g value from 2.0023 and often make it anisotropic, providing a fingerprint of the defect's local symmetry and bonding. In doped transition-metal (TM) oxide or semiconductor systems, this includes many native defects (oxygen or cation vacancies, trapped charge centers) and dopant ions(e.g. Cu^{+2}, Fe^{+3}, Ni^{+}, etc). Intrinsic defects are native to the host lattice (vacancies, interstitials, antisites), while extrinsic centers come from impurity atoms or intentional dopants. EPR can distinguish these by their characteristic g factors, hyperfine splittings, and by how signals change when the material is doped. For example, undoped ZnO often shows an isotropic line near $g \approx 2.00$ attributed to singly ionized Zn vacancy whereas intentional doping gives additional multi-line spectra from those ions (Jakes & Erdem, 2011). Likewise, in core–shell nanostructures or polycrystalline grains, EPR can separate surface (shell) vs bulk (core) defect signals: for instance, ZnO nanoparticles show two EPR lines with distinct g values ($g \approx 2.00$,$g \approx 1.96$) arising from defect sites on the surface and core, respectively (Parashar, Murty, Repp, Weber, & Erdem, 2012). Under a core–shell model, the $g \approx 1.96$ signal is generally associated with shallow donor states, most commonly assigned to singly ionized oxygen vacancies, though it has also been attributed to unpaired electrons localized at oxygen vacancies, ionized impurity atoms within the ZnO lattice, or even to delocalized free carriers in the conduction band (Jakes & Erdem, 2011). Thus EPR provides insight into whether paramagnetic defects are native or impurity-derived, and whether they lie near surfaces or in the bulk of grains/nanocrystals.

Two relaxation times govern EPR signals T_1 (spin–lattice relaxation) is the time for spins to exchange energy with the lattice and return to thermal equilibrium populations, while T_2 (spin–spin or transverse relaxation) is the time over which spin coherence dephases (Baumann et al., 2015). In a homogeneous ensemble with a single T_2, the EPR line has a Lorentzian profile whose width (half-width at half-max) is inversely proportional to T_2 . In effect, short T_2 produces broad lines and long T_2 narrows them. In solids and powders, however, inhomogeneous broadening is com-

mon: slight variations in local fields (e.g. strain, unresolved hyperfine fields, g-value anisotropy) cause a distribution of resonance frequencies. This yields a Gaussian or mixed (Voigt) line shape. In practice many defect-center signals are inhomogeneously broadened by lattice disorder; fitting a Voigt (Gaussian×Lorentzian) profile often decomposes the width into a homogeneous $\left(\sim \frac{1}{T_2}\right)$ part and a static (Gaussian) part.

Because EPR in solids often has both homogeneous and inhomogeneous contributions, lines are typically neither purely Lorentzian nor purely Gaussian. Under rapid passage (fast scanning) one sees mixed shapes (often fitted to a Voigt or a sum of Gaussian and Lorentzian). Unresolved hyperfine splitting or anisotropic g tensors also add shoulders or broadening. Notably, a purely homogeneous (Lorentzian) line implies all spins have identical environment and T_2, while a Gaussian component indicates a spread of environments. The relative Gaussian/Lorentzian contributions can change with temperature or sample state: for instance, motional narrowing at higher T can reduce inhomogeneous broadening making the line more Lorentzian-like.

In metallic or semiconductor hosts doped with TM ions, EPR reveals the local electronic structure of the defect. For instance, the g tensor anisotropy and hyperfine splitting of a transition-metal ion reflect the crystal-field symmetry and covalency of its site. In defective semiconductors (e.g. ZnO, TiO_2, etc.), EPR identifies specific vacancies or interstitials (each with characteristic g values) and shows how these change with doping. EPR can also detect interactions (exchange coupling) between spins: if defect spins interact strongly (e.g. in concentrated doping or metallic systems), their exchange can narrow and shift lines. In core–shell nanoparticles, as noted, EPR can separately monitor core vs surface defects, giving insight into how doping or processing affects the defect distribution. Overall, EPR's sensitivity to line shape, relaxation, and saturation makes it a powerful probe of the local magnetic fields and electronic structure at defect centers in transition-metal doped materials.

3.2 Photoluminescence (PL) Spectroscopy

Photoluminescence (PL) spectroscopy offers a noninvasive and contact-free approach to examine a material's electronic structure using light (Mitrić, 2022). When a sample absorbs photons, electrons are excited from their ground states into higher energy

levels called photoexcitation (Adams & Barbante, 2015). This photoexcitation triggers a sequence of relaxation events. Some excited electrons lose energy without emitting light while others recombine radiatively and release photons. Examination of the emitted light in terms of its wavelength, spatial origin, and time profile reveals the underlying electronic transitions and defect states (Adams & Barbante, 2015; Fick, 2001). Semiconductors and insulators with well defined energy levels offer clear PL signatures that are sensitive to intrinsic and extrinsic defect states. Unlike EPR, PL spectroscopy can identify a broad spectrum of defects, including structural vacancies, impurities, and surface adsorbates (Shukla & Bari, 2018).

In semiconductors and molecular systems, the energy of each emitted photon corresponds directly to the gap between occupied and unoccupied orbitals or bands (Erbe et al., 2018). By recording the spectral distribution of photoluminescence, one can determine the direct band gap of a semiconductor or the HOMO–LUMO gap in a molecule (Erbe et al., 2018). Likewise, radiative transitions that involve localized defect levels produce distinct emission lines allowing precise identification of impurity concentrations and vacancy or interstitial defects. At low temperatures, these defect-related peaks become sharper, enabling detection of trace impurities that critically affect device performance.

Beyond steady state measurements, PL can be performed in situ or operando during photocatalytic reactions and electrochemical cycling (Erbe et al., 2018). When applied to photocatalysis, PL reveals surface processes and charge-carrier dynamics at the semiconductor-liquid interface. In an electrochemical cell, tracking the evolution of the PL signal during oxidation or reduction offers real time insight into defect formation in oxide films. Such operando studies help to optimize catalyst performance and electrode stability.

Luminescence arises when absorbed energy is reemitted as photons. Photoluminescence is a subset of this phenomenon, initiated specifically by photon absorption. Instrumentation typically employs ultraviolet excitation sources such as xenon lamps or tunable lasers emitting near 254 nm. The choice of excitation wavelength depends on the material's absorption spectrum, one may select ultraviolet, visible or even near-infrared light to match the sample under study. Absorption of this radiation raises electrons to excited states; subsequent relaxation to the ground state emits photons in the visible range which are captured by sensitive photomultiplier detectors. By tuning the excitation wavelength and detection bandwidth, one can optimize the measurement for particular defect levels or trace impurities. Low temperature PL spectroscopy further enhances spectral resolution, revealing fine structure associated with impurity related emissions that would otherwise be

obscured at room temperature.

Recombination dynamics reflect the competition between radiative and nonradiative pathways (Shukla & Bari, 2018). The relative intensities and lifetimes of PL emissions quantify recombination rates. High radiative rates yield strong PL, whereas dominant nonradiative decay, often mediated by defects, diminishes the luminescent signal. Analysis of temperature and power dependent PL thus elucidates the mechanisms by which impurities and surface states influence carrier lifetimes and quantum efficiency.

PL spectroscopy, in summary, enables the noninvasive study of band gaps, the detection of impurity levels and excited-state behavior, and elucidation of recombination mechanisms supporting its indispensable role in evaluating semiconductors and investigating interfacial processes in electrochemistry.

4. METHODS

This section presents below the methods used to examine the structural, morphological, optical, and electrochemical properties of doped and undoped ZnS electrode materials synthesized via precipitation synthesis. The experimental workflow is broken down into seven subsections. The first subsection delineates the chemical precursors, doping strategies, and processing conditions used to obtain the nanostructured materials. The second subsection describes the XRD analysis, which was employed to confirm crystallinity, phase purity, and possible lattice distortions induced by doping. The third subsection provides information on SEM analysis, which revealed details of particle size distribution and microstructural features. The fourth subsection details the instrumental parameters of EPR spectroscopy, used to identify paramagnetic defects. Fifth, the PL spectroscopy setup is detailed to exhibit the band structure, identify defect-related emissions, and assess carrier recombination dynamics. Then, the fabrication of symmetric two-electrode cells is detailed, including electrode preparation, electrolyte selection, and overall cell configuration. Finally, the Electrochemical Analysis subsection presents the experimental parameters used in cyclic voltammetry (CV), potentiostatic electrochemical impedance spectroscopy (PEIS), and galvanostatic charge–discharge (GCPL) to assess capacitive behavior, charge transport dynamics, and internal resistance.

4.1 Materials and Synthesis

The precipitation synthesis employed here relies on the controlled nucleation and growth of ZnS-based nanoparticles in an aqueous medium. The present method introduces additional control over dopant incorporations by using tuned precursor ratios and surfactant-assisted mixing. This approach is particularly useful for achieving homogeneous vanadium doping in zinc sulfide matrices.

The synthesis begins by dissolving 16.5 mM of zinc acetate dihydrate ($Zn(CH_3COO)_2 \cdot 2H_2O$) and different molar concentrations of sodium metavanadate ($NaVO_3$) in 200 mL of double-distilled (DD) water under continuous and vigorous magnetic stirring at room temperature for 30 minutes. To this zinc precursor solution $NaVO_3$ is added at various concentrations (0.3, 0.5, 0.7, and 1 mol%) calculated based on the substitution of zinc ions in zinc acetate by vanadium ions, particularly for optimizing electrochemical performance while minimizing structural disruption. The precise stoichiometric replacement ensures systematic doping and reproducibility. The solution is continuously stirred to allow full dissolution of the metal salt and to facilitate pre-complexation, which is critical for the uniform incorporation of V^{+5} ions into the ZnS lattice during precipitation.

To improve particle dispersion and to minimize agglomeration during the growth phase, 1 gram of polyvinylpyrrolidone (PVP) is introduced into the reaction system as a surfactant and capping agent. PVP molecules adsorb on the nucleating ZnS particles, effectively controlling particle size and morphology by steric stabilization. The stirring is continued until the PVP is fully dissolved, yielding a clear and homogeneous precursor mixture.

In a separate vessel, 2 mM of thioacetamide (TAA, C_2H_5NS), a slow-release sulfur source, is dissolved in 100 mL of DD water. Thioacetamide is chosen for its ability to decompose gradually under heating, releasing sulfide ions (S^{-2}) in a controlled manner. This helps to avoid instantaneous nucleation, allowing for better crystallinity and controlled growth of the ZnS particles. The sulfur-containing solution is then added dropwise into the zinc/vanadium precursor solution. This dropwise addition is crucial to maintaining a controlled rate of sulfide ion introduction, which directly affects the supersaturation level and hence the nucleation rate. The dropwise addition also minimizes the local concentration gradients, which would otherwise lead to non-uniform nucleation and irregular particle shapes or sizes.

Once the addition is complete, the entire reaction mixture is transferred into a glycerin bath maintained at 100°C. The choice of a glycerin bath provides uniform heating and ensures a stable temperature environment without introducing sudden temperature gradients. This helps in achieving homogeneous thermal decomposition of TAA and consistent reaction kinetics across the whole volume. The mixture is stirred continuously in the bath for 2 hours, which allows the complete reaction of precursors and ensures the growth of doped ZnS nanoparticles to completion.

The precipitate obtained then washed several times with DD water to remove any residual ions, unreacted precursors, and loosely bound PVP. The multiple washing steps are essential to purify the product and to improve the performance of the ma-

terial in subsequent characterization. The purified product is then dried in a static oven at 70°C, which is sufficient to remove absorbed water and volatiles without altering the crystal phase or inducing agglomeration. The final powders obtained exhibit variations in vanadium doping concentrations, and for systematic study, the samples are labeled as ZnS:V X%, where X = 0, 0.3, 0.5, 0.7, or 1 mol% denotes the vanadium molar concentration relative to zinc.

The synthesis route is shown in Fig 4.1 . Firstly, the incorporation of PVP not only enhances colloidal stability but also provides better control over morphology and surface area, factors that are critically important in applications such as photocatalysis and energy storage. Secondly, the use of thioacetamide enables a sulfur-controlled, low-temperature synthesis, in contrast to high-temperature sulfide sources which often result in uncontrolled burst nucleation and poor crystallinity. Additionally, the moderate reaction temperature of 100°C and atmospheric pressure conditions simplifies synthesis setup. The reaction pathway also allows for systematic doping control, which is particularly important for evaluating structure-property relationships in ZnS-based materials doped with transition metals such as vanadium. Vanadium incorporation is expected to modulate the electronic structure, introduce localized states in the bandgap, and influence defect chemistry factors that are essential for tuning the electrochemical properties of ZnS.

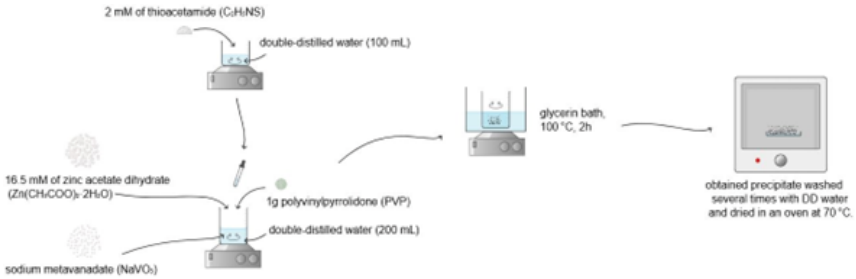

Figure 4.1 Schematic representation of the precipitation synthesis route.

4.2 X-Ray Diffraction Analysis

The crystalline structure and microstructural properties of the synthesized ZnS and V-doped ZnS samples were characterized using XRD. Measurements were performed on a Smart Lab Rigaku diffractometer with Cu-Kα radiation ($\lambda = 1.5406$). ll measurements were performed over a 2θ range of 20 to 90, with a 0.01 step size. The average crystallite size (d) was estimated using the Williamson–Hall method with

the equation:

$$\beta \cos\theta = \frac{k\lambda}{d} + 4\varepsilon \sin\theta \tag{4.1}$$

where β is the full width at half maximum (FWHM) of the diffraction peak (in radians) corrected for instrumental broadening, θ is the Bragg angle, k is the shape factor (taken as 0.9), and λ is the X-ray wavelength. The plot of $\beta\cos\theta$ versus $4\sin\theta$ was constructed, and the crystallite size was calculated from the intercept, while the slope provided ε the microstrain value. Rietveld refinement was employed to calculate lattice parameters from the XRD patterns and confirm the successful incorporation of vanadium into the ZnS lattice. Structural modifications induced by doping were quantitatively assessed through the refinement of lattice parameters and peak profiles.

4.3 UV-Vis Spectroscopy

The optical properties and band gap energies of the synthesized samples were investigated using ultraviolet–visible (UV–Vis) spectroscopy. The absorption spectra in the 200–800 nm spectral range were acquired using a JASCO V-570 UV–vis–NIR spectrophotometer, equipped with a JASCO ARN-475 accessory for absolute reflectivity measurements. UV–Vis analysis was performed to determine the materials' optical band gap, which is a key parameter influencing their electronic, photocatalytic, and electrochemical performance.

The optical band gap E_g was estimated using the Tauc method which relates the absorption coefficient (α) and photon energy ($h\nu$) as:

$$(\alpha h\nu)^n = A(h\nu - E_g) \tag{4.2}$$

where A is a constant, $h\nu$ is the photon energy, and n depends on the nature of the electronic transition (n = 2 for direct allowed transitions, n = 1/2 for indirect allowed transitions).

4.4 Scanning Transmission Electron Microscopy Analysis

The morphology and microstructure of the undoped and V-doped ZnS samples were examined using scanning transmission electron microscopy (STEM). Imaging was performed with a Hitachi HD-2700 microscope operated at 200 Kv. STEM analysis provided high-resolution images to evaluate particle size and shape coupled with energy-dispersive X-ray spectroscopy (EDS) to provide detailed elemental composition maps to confirm presence of Zn and S.

4.5 Electron Paramagnetic Resonance (EPR) Spectroscopy

Electron paramagnetic resonance (EPR) spectroscopy was performed at room temperature using a X-band Bruker E-500 ELEXSYS spectrometer operating at 9.8 GHz. EPR analysis was conducted to detect and characterize unpaired electrons and paramagnetic species present in the undoped and V-doped ZnS samples. This method was employed to provide insights into defect states, doping effects, and electronic environments, which are critical for understanding the materials' electronic structure and their influence on optical and electrochemical properties.

4.6 Photoluminescence (PL) Spectroscopy

PL spectroscopy was employed to investigate defect-related emissions and the influence of doping on emissions from defect centers in the sample. The sample was exposed to UV light, specifically at an excitation wavelength of 350 nm, which promoted electrons in the material to a higher energy state. PL spectra were measured using an FS5 spectrofluorometer (Edinburgh Instruments), equipped with a 150 W continuous-wave (CW) ozone-free Xenon arc lamp, a Czerny–Turner configuration with plane grating monochromators, and a PMT-900 emission detector. The samples were tested at room temperature in water-based solution. The excitation light source provided the energy to excite electrons, which then relaxed to a lower energy

state, emitting light as they returned to their ground state. The emitted light was collected and analyzed to provide insight into the material's electronic and optical properties. The emission wavelength was set to 360 nm, with a slit distance for both excitation and emission of 3.5 nm, allowing for detailed examination of the defect-related and doping-induced emissions in the sample.

4.7 Supercapacitor Design

Symmetric supercapacitor cells were fabricated using a two-electrode system, where both electrodes consisted of ZnS:V powders with varying vanadium concentrations (0, 0.3, 0.5, 0.7, and 1%) as shown in Table 4.1. Whatman glass microfiber membrane served as the dielectric separator, and 6 M KOH was employed as the electrolyte. For device assembly, two identical electrodes, prepared from either undoped or V-doped ZnS, were positioned face-to-face, separated by the electrolyte-soaked glass fiber filter shown in Fig 4.2 No binder or conductive additive was used in the electrode formulation. The electrode pair, with the separator in between, was mechanically compressed into a pellet using screws and metal current collectors on both sides to ensure electrical contact and device stability during testing.

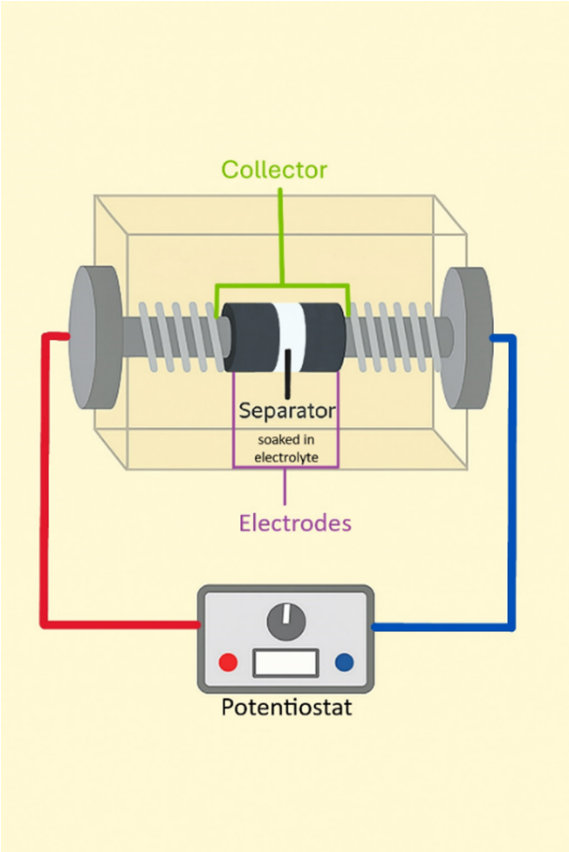

Figure 4.2 Depiction of the double-electrode symmetric supercapacitor configuration used to evaluate the supercapacitive performance of the ZnS-based materials.

Table 4.1 Cell components of each supercapacitor device.

Device Code	**Electrode Material 1**	**Electrode Material 2**	**Electrolyte**	**Type**
SC1	ZnS:V 0%	ZnS:V 0%	6 M KOH	Symmetric
SC2	ZnS:V 0.3%	ZnS:V 0.3%	6 M KOH	Symmetric
SC3	ZnS:V 0.5%	ZnS:V 0.5%	6 M KOH	Symmetric
SC4	ZnS:V 0.7%	ZnS:V 0.7%	6 M KOH	Symmetric
SC5	ZnS:V 1%	ZnS:V 1%	6 M KOH	Symmetric

4.8 Electrochemical Measurements

The electrochemical performance of the ZnS:V samples were evaluated to determine their suitability for supercapacitor applications. All measurements were conducted using a symmetric two-electrode configuration to investigate both electrode-

electrolyte interaction and the mutual influence of the electrode materials. Each test device was constructed identically, with the active material uniformly distributed on a stainless-steel disc-shaped current collector with a mass loading of 2.5 mg. This mass was selected to align with commonly reported values in the literature while also delivering reliable electrochemical responses.

The assembled symmetric devices were connected to a VMP-300 multichannel potentiostat (BioLogic, France), and all electrochemical measurements were performed at ambient temperature. A variety of characterization techniques were employed to assess capacitive behavior, including cyclic voltammetry (CV), which applies a linear potential sweep to evaluate redox activity, specific capacitance, and long-term cycling performance. Additionally, potentiostatic electrochemical impedance spectroscopy (PEIS) was conducted to analyze frequency-dependent response, while voltage holding (VH) and galvanostatic charge-discharge (GCPL) tests were performed to further probe the stability and charge storage characteristics of the devices.

4.8.1 Cyclic Voltammetry (CV)

CV was utilized in this study to explore the electrochemical properties of the fabricated SC devices. As a widely adopted technique in electrochemical analysis, CV offers insight into the redox characteristics, charge storage capacity, and operational stability of electrode materials. The process involves applying a time-dependent, linearly varying voltage to the working electrode while measuring the resulting current. This current-voltage relationship reflects various electrochemical processes occurring at the electrode-electrolyte interface, including electron transfer reactions and ion movement. By examining the shape and symmetry of the CV curves, it is possible to assess how efficiently the material supports charge/discharge processes and whether those processes are predominantly capacitive or involve faradaic contributions. In this work, CV tests were conducted in a voltage range of 0 to +1 V at multiple scan rates, specifically 1, 5, 10, 20, 50, 100, and 200 mV/s. Performing the measurements at different scan rates helps in identifying how the device responds under varying charge/discharge conditions, which is critical for evaluating rate capability and charge transport mechanisms. The area enclosed by each CV loop was used to estimate the specific capacitance of the device, which is a measure of its ability to store charge.

$$C_s = \frac{A}{2mk\Delta V} \tag{4.3}$$

where A is the area under the CV curves, m is the total mass of electrode material, k is the scan rate, and ΔV is the voltage window. A larger enclosed area typically indicates improved energy storage performance. Beyond this, to further dissect the underlying charge storage processes, the Dunn method was employed. This approach helps in distinguishing between two primary mechanisms: one governed by rapid ion adsorption on the electrode surface (capacitive behavior typical of electric double-layer capacitors), and another driven by slower redox reactions involving diffusion into the bulk of the material (characteristic of pseudocapacitance). By analyzing the variation of current with scan rate in a logaritmic plot and interpreting the slope and intercept, it becomes possible to quantitatively separate these two contributions. This mechanistic understanding is particularly useful in evaluating the role of V doping in the electrode material, as it can influence both the capacitive and diffusion-controlled charge storage pathways. The current response can be described using the Equation 4.4 :

$$i_p(v) = k_1 v + k_2 v^{1/2} = i_{\text{capacitive}} + i_{\text{diffusive}} \tag{4.4}$$

where k_1 corresponds to the slope found via linear fit, and k_2 reflects intercept of the linear fit. By plotting the current against the square root and linear terms of scan rate, the proportion of each mechanism is determined through the plot's slope and y-intercept.

Overall, CV combined with the Dunn analysis, provides a comprehensive picture of the electrochemical behavior and charge storage dynamics of the SC devices under investigation.

4.8.2 Potentiostatic Electrochemical Impedance Spectroscopy (PEIS)

The PEIS measurements were carried out by applying a 10mV sinusoidal signal across a frequency range of 10Hz to 1MHz. The impedance behavior of both symmetric and asymmetric supercapacitors (SCs) was analyzed using electrochemical impedance spectroscopy (EIS), where the real part of the impedance was plotted against the negative imaginary part to produce Nyquist plots. According to existing literature, the intercept on the x-axis in the high-frequency region of the Nyquist plot corresponds to the internal or equivalent series resistance (ESR), which encompasses the resistances of the electrode, electrolyte, and the contact resistance at the electrode–current collector interface. The semicircle diameter in the high-frequency

region is indicative of the charge transfer resistance. Meanwhile, the inclined line at low frequencies represents the Warburg impedance, which reflects ion diffusion within the electrode material and the electrolyte. This Warburg element, also known as the transmissive diffusion element, plays a key role in determining the performance and cycling durability of symmetric and asymmetric SC systems.

4.8.3 Galvanostatic Charge–Discharge with Potential Limitation (GCPL)

The galvanostatic charge-discharge with potential limitation (GCPL) technique was utilized within the potential window of 1 to +1 V at a specific current of 0.1 A/g to evaluate the electrochemical stability of the supercapacitor samples. In this method, a constant current is applied during both charging and discharging processes, while the voltage is constrained within predefined upper and lower limits, at which the current direction is reversed or the process is terminated.

The energy density (E_d) can be determined using the Equation 4.5:

$$E_d = \frac{1}{2} C_s \Delta V^2 \tag{4.5}$$

where C_s represents the specific capacitance and ΔV is the applied potential window(1V). The power density (P_d) can be calculated by dividing the energy density (E_d) by the discharge time (Δt), which was obtained from the GCPL measurements for each device using:

$$P_d = \frac{E_d}{\Delta t} \tag{4.6}$$

5. RESULTS AND DISCUSSION

5.1 X-Ray Diffraction Analysis

The XRD analysis investigated the sample's structure and phase purity. As shown in Fig. 5, the diffraction pattern is composed by three peaks which can be attributed the reflection on the lattice planes (111), (220) and (311) of a sphalerite structure according to ICCD: 01-071-4763. No supplementary peaks are present, demonstrating the high purity of the ZnS samples. The broad diffraction lines are an indication of small crystallite sizes.

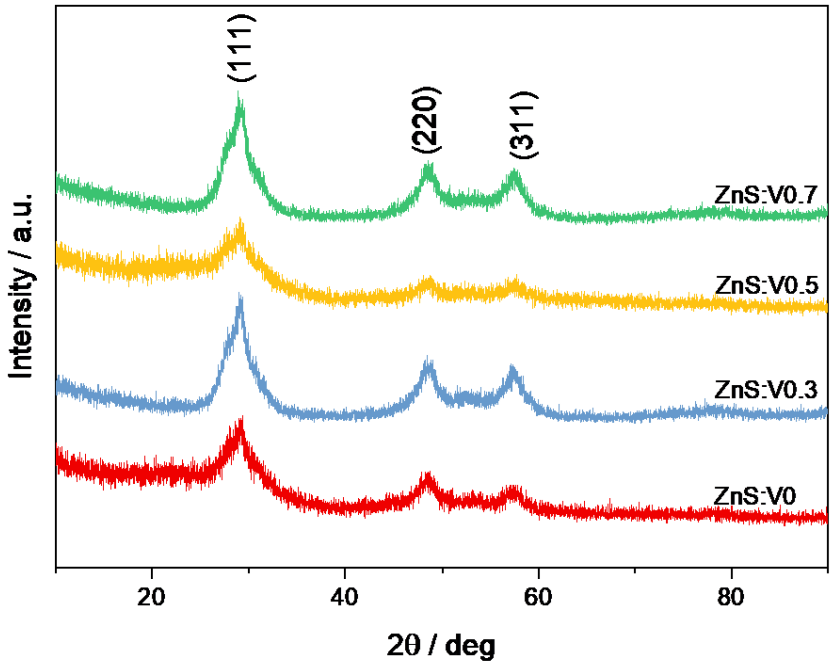

Figure 5.1 XRD diffractogram of the undoped and V-doped ZnS material.

The lattice parameters were calculated by Rietveld refinement and the crystallite

size by Williamson-Hall method. Since the ionic radius of the $V^(+2)$ ions (0.79 Å) is slightly larger than that of the Zn^{+2} ions (0.74 Å), a modification of the crystal lattice parameters and its volume is expected. The evolution of the lattice parameters, unit cell volume, and crystallite size with the dopant ion concentration is presented in Table 5.1. An increase in the unit cell volume of the doped samples is observed compared to the undoped ones. The crystallite size d varies between 1.5 and 3.7 nm, increasing with doping. Correlating these results with those obtained in XRD, we can conclude that the ZnS nanoparticles are polycrystalline.

Table 5.1 XRD-derived lattice parameters, unit cell volumes, and crystallite sizes for ZnS and ZnS:V samples

Sample	**a = b = c (Å)**	**V (Å^3)**	**d (Å)**
ZnS	5.272(2)	146.56	15
ZnS:V 0.3%	5.3500(9)	153.13(5)	24
ZnS:V 0.5%	5.086(7)	131.6	11
ZnS:V 0.7%	5.2827(6)	147.43	37

5.2 UV-Vis Spectroscopy

To examine the influence of V doping on the ZnS optical properties, UV-VIS spectroscopy was performed. Fig 5.2. illustrates the absorption spectra of undoped and V-doped ZnS. The undoped sample exhibits an absorption maximum located at 326 nm which is slightly shifted for V doped ZnS samples. The band gap energy was evaluated based on the Tauc equation (Lindon et al., 2016) and the obtained values are show in Fig 5.3. inset. The ZnS band gap (3.40 eV) is lower compared with ZnS bulk (3.7 eV) (Alam et al., 2024) which can be a consequence of structural defects generation during the synthesis process (Adachi, 1999). By 0.5% V doping a reduction of the band gap energy is observed explained by the sp–d exchange interactions causing shifts in the conduction and valence band edges (Baumann et al., 2015). By increasing the dopant concentration, a slight increase of the band gap energy is observed. This behavior can be attributed to the Burstein–Moss effect, which causes the Fermi level to shift toward the conduction band (Parashar et al., 2012).

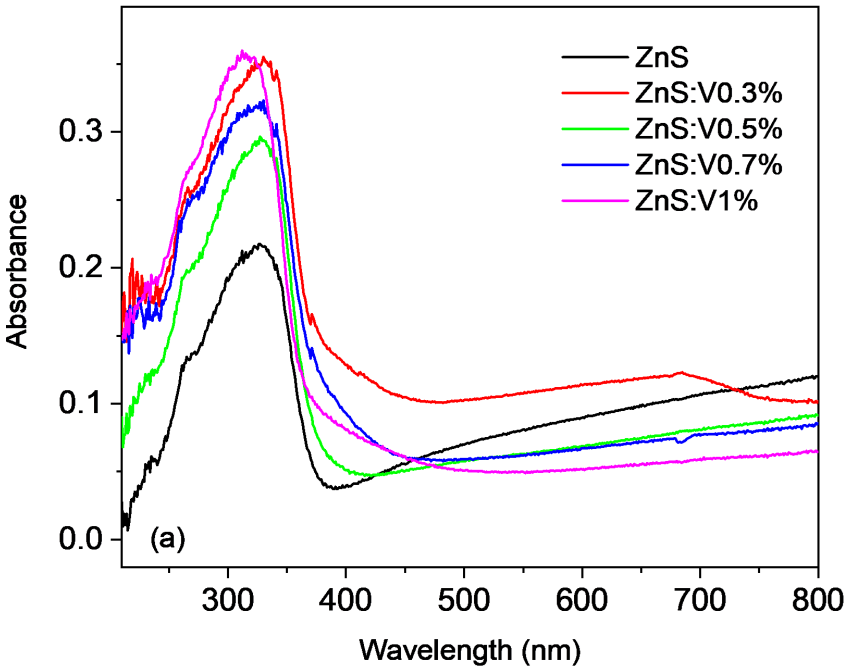

Figure 5.2 Absorption spectra of undoped and V-doped ZnS nanoparticles.

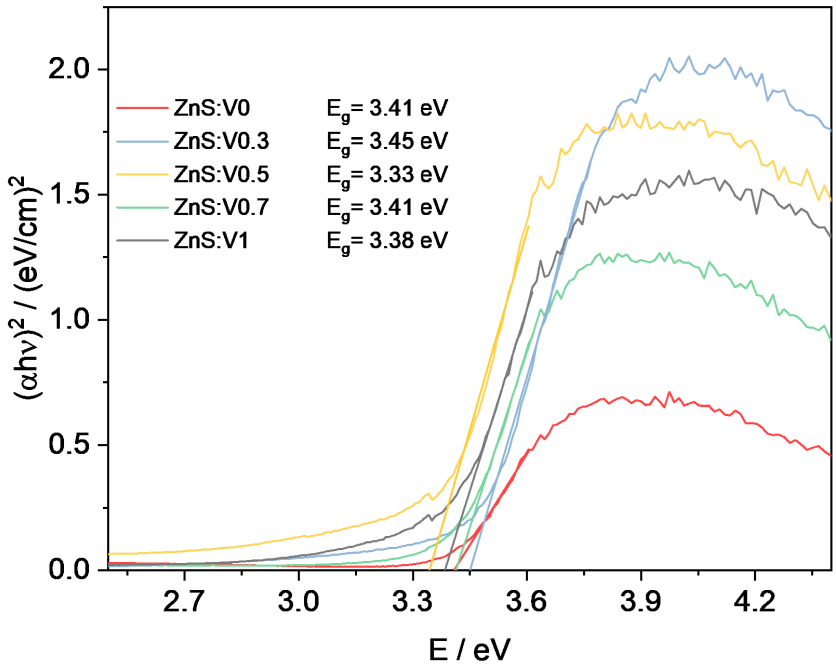

Figure 5.3 The band gap energy evaluated based on the Tauc equation.

5.3 Scanning Transmission Electron Microscopy Analysis

To investigate the morphology of the synthesized samples, STEM measurements were performed. Moreover, an elemental analysis was performed to show the samples' constituent elements, and elemental distribution maps were obtained. As shown in Fig 5.4, well-dispersed particles with a spherical shape were obtained with an average particle size of 70 nm. The elemental map confirms the presence of the two elements: Zn and S.

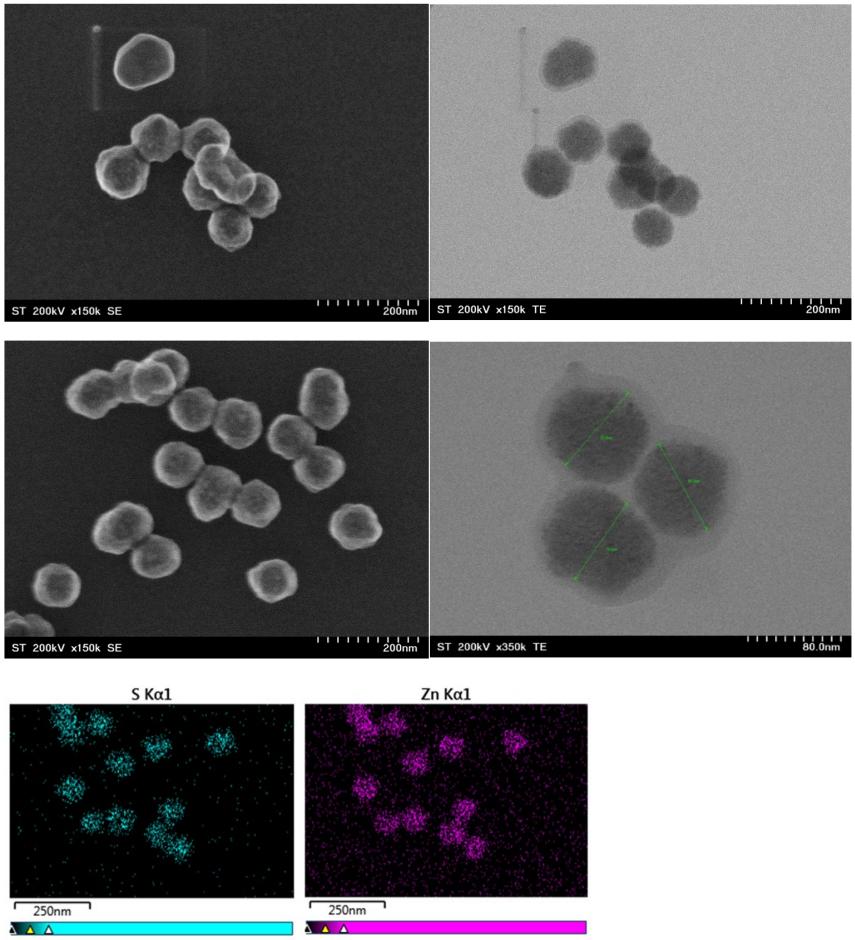

Figure 5.4 STEM micrographs and elemental distribution maps of undoped ZnS nanoparticles.

5.4 Electron Paramagnetic Resonance (EPR) Spectroscopy

EPR spectroscopy was conducted on doped and undoped ZnS nanoparticles to verify the incorporation of V ions into the ZnS lattice by identifying defect states and doping effects, which are key to understanding the material's electronic structure and its impact on electrochemical performance. The ZnS sample shows a broad resonance signal that has been previously observed in other materials and is attributed to a ferromagnetic phase in Fig 5.5 (Owens, 2005; Stefan et al., 2016). Superimposed on this is a narrow signal centered at g = 2.003 that has been attributed to monoionized zinc vacancies in ZnS QDs(Reddy et al., 2011).

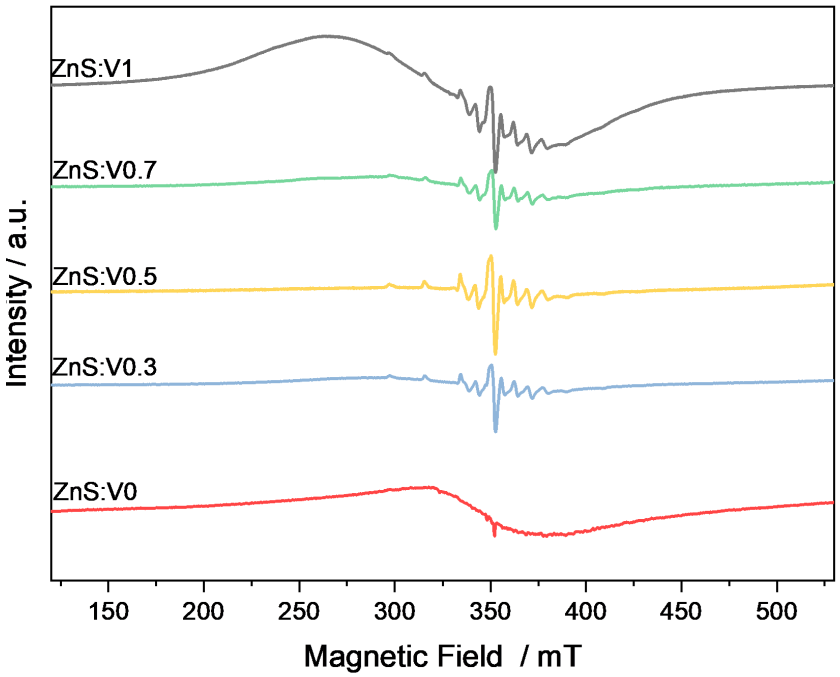

Figure 5.5 X-band spectra of undoped and V-doped ZnS samples.

The presence of the V ion in the ZnS crystal lattice is confirmed by EPR spectroscopy. The spectrum shows a characteristic complex structure of 16 lines with 8 parallel and 8 perpendicular lines. The electronic configuration of the V^{+4} ion is $3d^1$ and the only naturally stable isotope is 51V, which has a nuclear spin of I=7/2. The hyperfine components are typical for the interaction between the unpaired $3d^1$ electron and the 51V isotope in an axially distorted crystal field (Ardelean, Cozar, Vedeanu, Rusu, & Andronache, 2007). These spectra are described by the following spin Hamiltonian(Gahlot et al., 2005):

$$H_s = g_{\parallel}\beta B_z \hat{S}_z + g_{\perp}\beta(B_x\hat{S}_x + B_y\hat{S}_y) + A_{\parallel}\hat{I}_z\hat{S}_z + A_{\perp}\beta(\hat{I}_x\hat{S}_x + \hat{I}_y\hat{S}_y) \tag{5.1}$$

where β is the Bohr magneton; B_x, B_y and B_z are the static magnetic fields; $\hat{S}_x$, $\hat{S}_y$ and $\hat{S}_z$ are the electron spin operators (S=1/2); $\hat{I}_x$, $\hat{I}_y$ and $\hat{I}_z$ are the nuclear spin operators (I=7/2); and$g_{\|}$ and $g_{\perp}$ are the parallel and perpendicular components of the factor; $A_{\|}$ and $A_{\perp}$ are the parallel and perpendicular components of the hyperfine tensor.

As the vanadium ion concentration increases in the samples, in addition to the hyperfine structure due to isolated vanadium ions, a broad line due to dipolar interacting vanadium ions appears.

5.5 Photoluminescence (PL) Spectroscopy

The optical properties of the synthesized pure and V-doped ZnS samples were examined using PL spectroscopy. Unlike EPR, which is limited to detecting paramagnetic defects, PL is sensitive to a wide range of defects, making it a powerful tool for identifying structural imperfections. PL analyses were carried out on the prepared ZnS:V samples to examine the processes of charge carrier (electron and hole) generation and recombination. Fig 5.6 presents the PL spectra of ZnS samples synthesized with different vanadium doping concentrations (0, 0.3, 0.5, 0.7, and 1%), along with the deconvolution of the peaks highlighting various emission regions. The spectra for all samples were recorded at an excitation wavelength of 350 nm. Each sample's PL spectrum displays emission peaks of UV, blue, and green, and orange. After doping level reaches 0.5%, red emission is also observed. The peaks in the range of 440 nm–460 nm are attributed to blue emission, while those between 460 nm and 500 nm correspond to green emission. Each sample containing different vanadium concentrations displays structural defects, a common characteristic of nanomaterials.

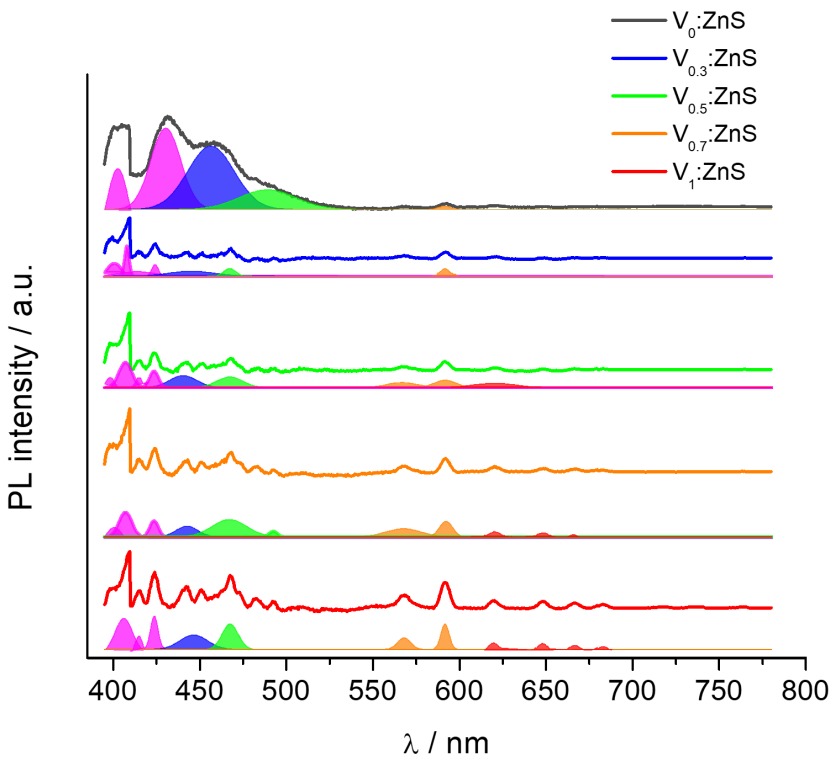

Figure 5.6 The PL spectra of ZnS samples synthesized with different vanadium doping concentrations (0, 0.3, 0.5, 0.7, and 1%), along with the deconvolution of the peaks.

Due to the broad and asymmetric nature of the spectra, they likely comprise multiple components. Therefore, Gaussian fitting was performed to separate the individual peaks within the PL spectra. The emission peak observed at 410 nm is attributed to the recombination process involving sulfur vacancy-related donor states and the valence band (S. Lee et al., 2004). Although various studies have attributed the 450 nm emission peak to different mechanisms depending on the dopant type, in this study, it is proposed that the 450 nm peak arises from intrinsic defect states rather than vanadium-related impurity states, as the undoped sample showed no presence of vanadium or other impurities. In ZnS nanoparticles, luminescence near 450 nm has also been linked to emissions from trap states associated with intrinsic zinc vacancies (Ahmad et al., 2025). The blue shift observed in the green emission of vanadium-doped ZnS nanoparticles as the vanadium content increases can be attributed to modifications in the local crystal field and electronic surroundings. These changes affect the energy gap between defect levels and the conduction or valence bands, resulting in emission at shorter wavelengths. The broad peak in the visible range can be attributed to extrinsic defects introduced by vanadium doping and the recombination of electron-hole pairs. The first PL peak intensity gradually decreases in the ZnS:V samples compared to pure ZnS. Such quenching is a common

phenomenon in chalcogenide-based nano-compounds, and it is influenced by the doping concentration. The reduction in PL intensity in V-doped ZnS, as opposed to the pure ZnS sample, can be due to lower recombination of charge carriers, resulting in increase of the performance (Hroub et al., 2023). However, beyond a 1% vanadium doping concentration, the emission intensity increases due to enhanced radiative recombination. The red emissions are weak or absent in undoped ZnS but become dominant in heavily doped samples, especially ZnS:V 1%. This suggests that V doping introduces a new, deep energy level within the bandgap. Based on these PL results, the high charge carrier density in ZnS:V suggests its potential for use in supercapacitor applications.

5.6 Electrochemical Measurements

5.6.1 Cyclic Voltammetry (CV)

CV was applied in this research to assess the electrochemical behavior of the prepared SC devices. Recognized as a standard tool in electrochemical studies, CV enables a detailed examination of the redox performance, charge storage capabilities, and stability of electrode materials during operation (Yamada, Yoshii, Asahi, Chiku, & Kitazumi, 2022). This method consists of delivering a voltage that changes linearly over time and recording the resulting current response. The relationship between current and voltage reveals important information about the electrochemical phenomena occurring at the interface between electrode and electrolyte, such as ion mobility and electron transfer processes (Forouzandeh et al., 2020). Through an evaluation of the CV curve profile and its symmetry, it is possible to interpret how well the electrode material handles the charging and discharging events, and to understand the involvement of capacitive and Faradaic mechanisms. In the present study, CV experiments were carried out using a range of scan rates from 1 to 200 mV/s. Examining the device response at these varied scan rates helps identify its charge-discharge performance under different electrochemical stress conditions, which is essential for understanding its rate capability and ion/electron transport efficiency. Fig 5.7. illustrates the CV profiles for each of the SC device configurations. The data represent the fourth cycle for all configurations. The CV shapes resemble

tapered quasi-rectangles, deviating from the ideal rectangle typically linked with EDLC-type storage behavior. In EDLCs, charge storage occurs via non-faradaic physical adsorption at the interface, resulting in ideal rectangular CV shapes. This EDLC mechanism relies on the fast movement of ions within the inter-electrode gap. The obtained curves suggest the coexistence of EDLC and pseudocapacitive processes. Such Faradaic activity is attributed to ion transport kinetics, indicative of pseudocapacitive characteristics. In the literature, cyclic voltammetry CV of ZnS demonstrates Faradaic processes, where energy is stored through the oxidation of ZnS to Zn^{+2} ions during charging, accompanied by the reduction of hydroxide ions. During discharge, Zn^{+2} ions are reduced back to ZnS, releasing energy through the oxidation of hydroxide ions. Using a voltage window of 0–0.6 V more clearly reveals the redox peaks associated with these reactions (Ahmad et al., 2025). This dual behavior stems from the synergy between fast surface adsorption and slower redox processes that occur within the material.

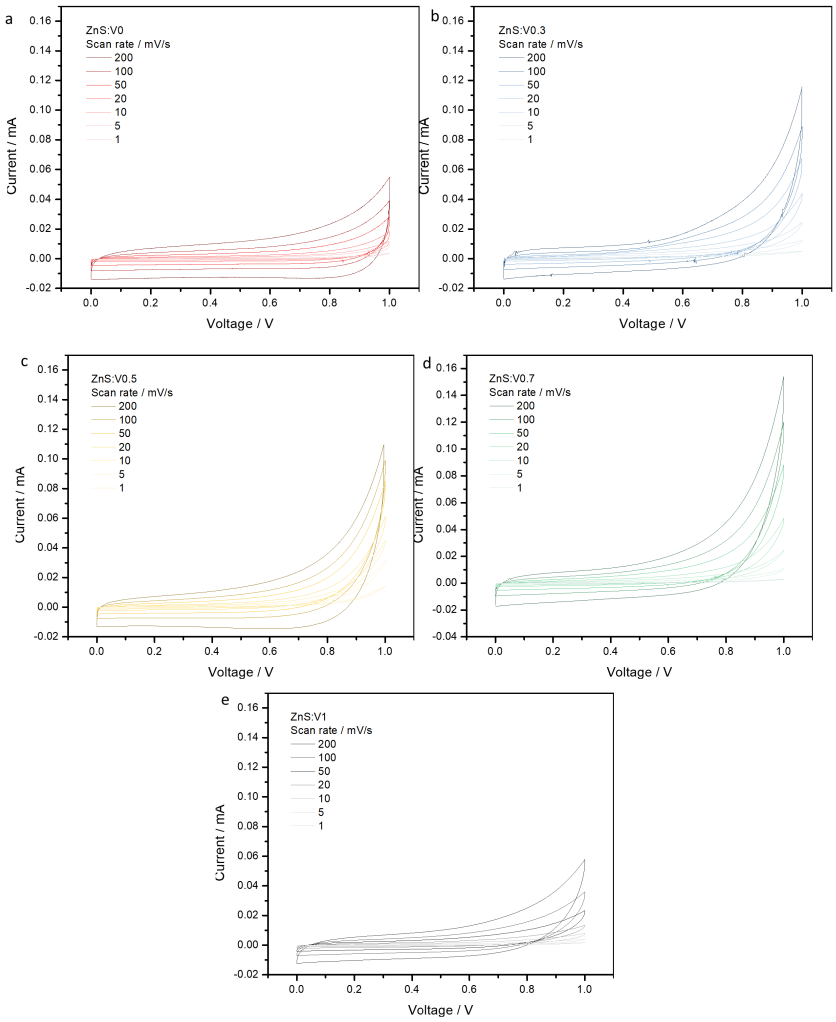

Figure 5.7 Cyclic Voltammetry of symmetric SC devices carried out between 0-1 V with scan rates are presented at inset where undoped ZnS (a), ZnS:V 0.3% (b), ZnS:V 0.5% (c), ZnS:V 0.7% (d), ZnS:V 1% (e).

The current response between forward and reverse voltage sweeps is not entirely symmetric; however, SC3 and SC4 show relatively better symmetry. Increased current in the forward scan, particularly at elevated scan rates, indicates pseudocapacitive contributions. In SC2, a minor hysteresis effect is visible. Across all tested devices, a gradual and curved increase in current, especially beyond approximately 0.8 V, points to capacitive charging along with surface-limited Faradaic activity, implying pseudocapacitive storage. Fig 5.8 further shows that all V-doped samples, except SC5, outperform the undoped SC1. Among them, SC4 delivers the highest current, followed by SC3 and SC2. These results suggest that vanadium doping enhances capacitance performance, while SC5 shows an exception. The way in which the materials were synthesized plays a key role in shaping their capacitive performance even when the composition remains unchanged. Variations in defect formation and control may provide a possible explanation for these outcomes.

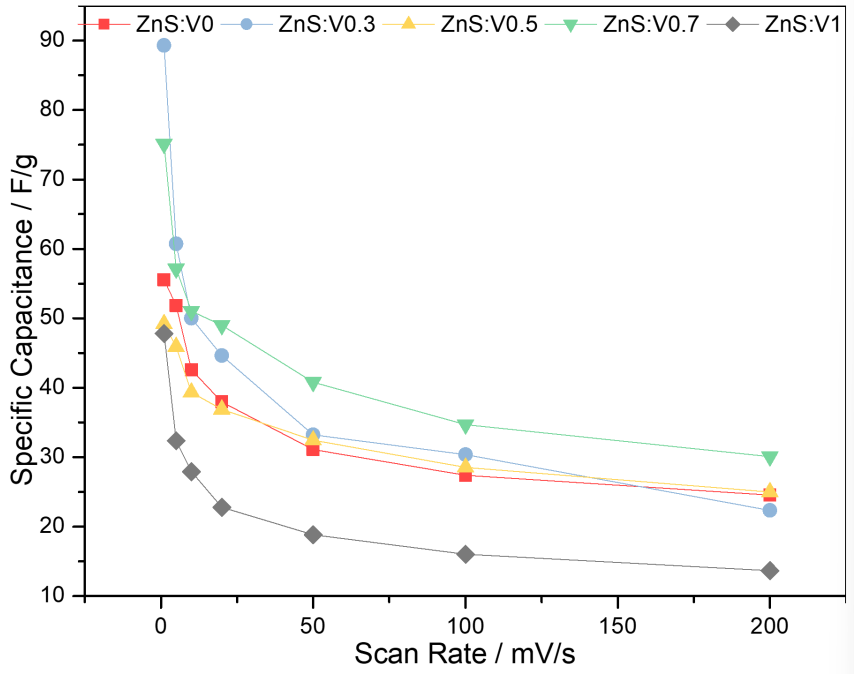

Figure 5.8 Specific capacitance evolution as a function of scan rate obtained from CVs.

The loop area captured in each CV scan was used to compute the device's specific capacitance, offering a quantitative measure of its charge storage efficiency. Generally, a larger area enclosed by the curve is associated with a higher energy storage capacity due to Equation 4.3. As shown in Fig 5.8. at a scan rate of 1 mV/s, SC2 with 90 F/g and SC4 with 75 F/g achieved significantly higher specific capacitance values compared to SC1, which exhibited 55 F/g. The most pronounced impact of doping is seen in the SC2, SC3, and SC4 samples. With vanadium concentrations of 0.3%, 0.5%, and 0.7%, respectively, the redox peaks become more distinct,

suggesting that V enhances redox activity by introducing additional reactive sites. However, as the doping level approaches 1%, this optimal range is surpassed. Although the peaks remain sharp, it is not due to an increase in redox activity; rather, the emergence of ionic resistance begins to hinder performance, leading to a decline in both peak current values and specific capacitance.

To further interpret the charge storage dynamics, Dunn's method was implemented using Equation 4.4. The Dunn method enables the identification of charge storage mechanisms in supercapacitor systems by distinguishing between two primary processes: a capacitive response driven by fast ion movement at the electrode interfaces in electric double-layer capacitors (EDLCs), and a diffusion-controlled process involving Faradaic reactions, which can further enhance device performance by contributing additional redox activity (Shreya, Phogat, Jha, & Singh, 2023).

Due to the lack of well-defined redox peaks in the voltammogram, this approach is applied to highlight the impact of diffusion-based Faradaic processes. Findings indicate in the Fig. 13. that at 5 mV/s scan rate, the diffusive contribution reaches approximately 60% in the SC2 sample and 80% in the SC3 sample while it remains at 50% for SC1, indicating a significant pseudocapacitive behavior. Lower scan speeds are preferred in this context as they allow adequate time for redox interactions to take place. As such, diffusion-related mechanisms tend to dominate at slower scan rates, whereas capacitive effects prevail when the scan rate increases, due to the faster ion transport dynamics.

Vanadium ions exhibit multiple oxidation states (V^{+2}, V^{+3},V^{+4}, V^{+5}), endowing the system with inherent redox activity (Zhu et al., 2025). When vanadium is incorporated into the ZnS crystal lattice, it creates redox-active centers capable of reversible electron transfer during charge and discharge cycles. These oxidation state transitions (e.g., V^{+2}/V^{+3}, V^{+3}/V^{+4}, V^{+4}/V^{+5}) facilitate Faradaic reactions both at the surface and within the near-surface regions of the electrode, thus enabling rapid and reversible redox-based charge storage beyond mere surface ion adsorption, ultimately boosting electrochemical performance through deeper and faster redox reactions. This assumption is supported by the Dunn method analysis, which shows a progressive increase in diffusive contribution with rising vanadium content, indicating enhanced bulk redox activity and ion transport. The trend continues up to ZnS:V 0.7%, suggesting that moderate doping effectively promotes pseudocapacitive behavior. However, at 1% V content, a slight decline in diffusive contribution is observed.

Additionally, doping ZnS with vanadium generates sulfur vacancies within the material's structure (Guo et al., 2024). These vacancies enhance electrical conductivity

and offer extra active sites for redox interactions with electrolyte ions by serving as accessible pathways or anchoring points. Since the PL results showed a decrease in the 420 nm peak intensity which is attributed to sulfur vacancy-related recombination, the enhancement in diffusive behavior can be attributed to the incorporation of vanadium into the ZnS lattice and the generated sulfur vacancies, which creates redox-active centers.

In conclusion, the enhancement of the diffusive mechanism in ZnS:V at doping levels of 0.3%, 0.5%, and 0.7% is mainly due to the increased number of charge carrier sites introduced by vanadium atoms, which amplify Faradaic reaction contributions. However, when the doping level reaches 1%, the performance tends to decline, possibly because excessive vanadium causes lattice distortion, dopant clustering, or saturation of active sites (Rana et al., 2021). These structural issues hinder effective electrochemical reactions and reduce the efficiency of diffusion-controlled charge storage mechanisms.

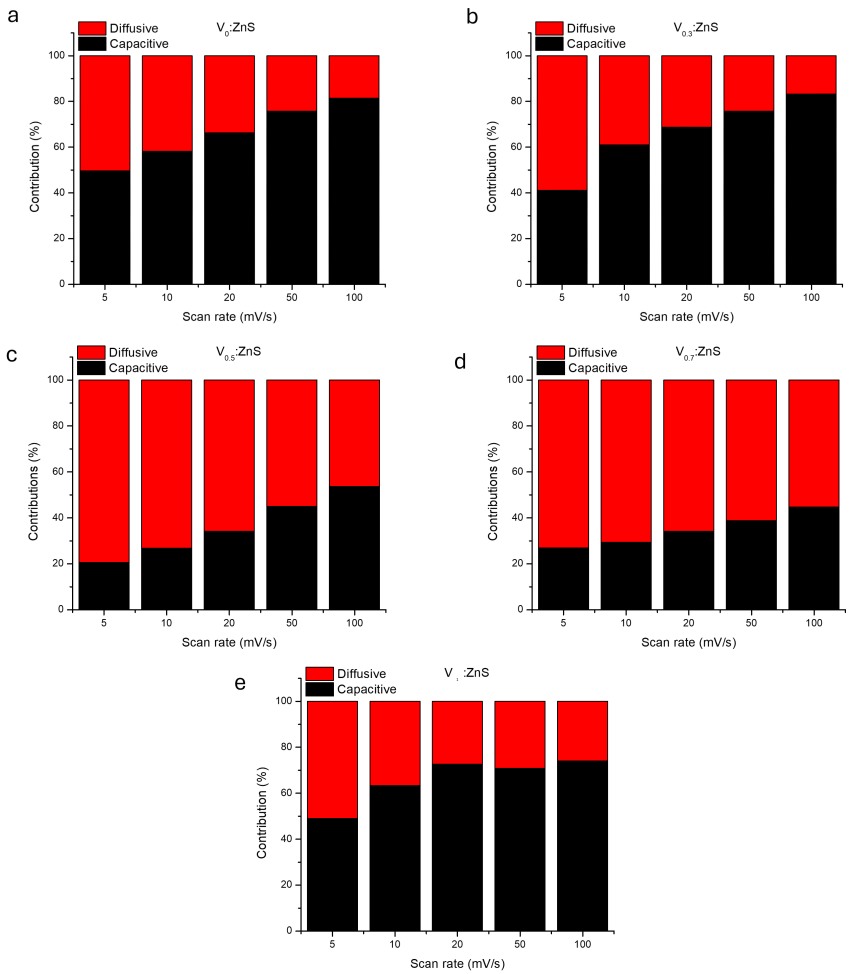

Figure 5.9 Capacitive and diffusive contribution analysis of undoped ZnS (a), ZnS:V 0.3% (b), ZnS:V 0.5% (c), ZnS:V 0.7% (d), ZnS:V 1% (e) using Dunn Method.

5.6.2 Potentiostatic Electrochemical Impedance Spectroscopy (PEIS)

PEIS serves as a fundamental diagnostic tool for evaluating the electrical behavior of SC systems. It offers detailed information regarding charge transport dynamics, resistive and capacitive elements, as well as interfacial mechanisms that are critical for the enhancement of material performance. The impedance responses are illustrated in Table 5.1. with the equivalent circuit R1+(Q2/R2)+(Q3/(R3+W3)). Z-fit was carried out on the impedance data to get further insight into the resistance values of the SC devices shown in Fig 5.10. Analysis of the Nyquist plots and their corresponding equivalent circuit models confirms the occurrence of multiple charge transfer phenomena. These typically involve the electrode–electrolyte interface, interfacial resistances, and ion diffusion constraints, evident from the Warburg element's appearance as a linear tail in the low-frequency region, indicating mass transport as the dominant limiting factor over charge transfer or capacitive storage (Huang, 2018). R1 is the high-frequency intercept on the Nyquist plot, reflecting the equivalent series resistance of the device. It includes the intrinsic electrode resistance, electrolyte ionic resistance, and contact resistances in the cell. A lower R1 indicates better electrical conductivity and less internal voltage drop, which is critical for high power output and low ohmic losses (Lazanas & Prodromidis, 2023). R2 corresponds to the diameter of the first high-frequency semicircle in the Nyquist plot. It represents the charge transfer resistance at the electrode/electrolyte interface for fast processes such as the double-layer charging or any rapid Faradaic reactions. A smaller R2 implies more facile charge transfer kinetics and thus less voltage lag during rapid charging/discharging (Choi, Shin, Kim, Choi, & Yoon, 2020). R3 represents a second, lower-frequency resistive process. In supercapacitors, this can be associated with Faradaic pseudocapacitive reactions or leakage pathways. A lower R3 suggests easier charge transfer for slower processes. R3 can also capture self-discharge or resistive losses that bleed charge at longer times (Vivier & Orazem, 2022). Q2 is a constant phase element modeling the non-ideal double-layer capacitance at the electrode interface. Ideal double-layer capacitors would show a pure capacitance, but real electrodes exhibit dispersion due to surface roughness, porosity, and inhomogeneous current distribution. Q3 is the constant phase element paired with R3, representing the capacitance of the slower process. This often corresponds to pseudocapacitive or additional capacitive behavior beyond the electric double-layer, for example, redox reactions at dopant sites or intercalation processes that contribute to capacitance. A high Q3 value indicates substantial pseudocapacitive charge storage (Panchu, Raju, & Swart, 2024). In the context of vanadium doping, Q3 can be viewed as the faradaic pseudocapacitance introduced by vanadium

redox reactions or defect-induced charge storage sites. Essentially, doping with a redox-active element like V can add a battery-like capacitance component, raising Q3 significantly compared to the undoped material. The Warburg Diffusion Element W accounts for ionic diffusion limitations in the electrode, observed as a 45° sloping line in the low-frequency region of the Nyquist plot (Huang, 2018). Physically, W reflects the resistive impedance increase when ions must diffuse into porous electrodes or to faradaic sites. A smaller Warburg coefficient indicates more facile ion transport (short diffusion paths or fast ion diffusion), whereas a large W suggests significant diffusion constraints (e.g. microporous structure or slow diffusion through the material) (Azizpour et al., 2025).

Since ZnS is a wide-bandgap semiconductor with relatively poor intrinsic conductivity, the electron transport might be limited and slowing down redox reactions at the electrode surface. In general, increasing the V doping level progressively lowers the resistive components (R1, R2, R3) and increases the pseudocapacitive element (Q3), while reducing the Warburg impedance. This indicates that vanadium doping substantially improves the electrode kinetics and charge storage capability.

SC1 exhibits the highest internal resistance R1 and the largest charge-transfer resistance R2, reflecting slower interfacial kinetics. The pseudocapacitance Q3 is minimal showing limited faradaic contribution, and the Warburg element W is relatively high. These impedances hinder charge storage, leading to the lowest specific capacitances among the series.

SC2 shows a modest reduction in R1 and R2 compared to SC1, indicating improved electrical conductivity and slightly faster charge transfer. Q3 rises, signifying that introducing a small amount of V begins to activate pseudocapacitive behavior. The Warburg impedance also decreases, implying easier ion diffusion. Specific capacitances increase accordingly which was shown in Fig 5.7.

SC3 shows that doping at 0.5% yields a significant drop in both R1 and R2. In fact, studies on ZnS have found that doping can dramatically lower the series resistance and charge-transfer resistance, improving electrode kinetics. Here Q3 is substantially higher showing greater pseudocapacitance from faradaic reactions and W is further reduced indicating diminished diffusion limitations. These changes reflect a much more electrochemically active and conductive electrode.

SC4 confirms the trend. SC4 achieves comparably low R1/R2 and high Q3 where SC5 continues the trend of reduced resistances, R1 and R2 are the lowest of all samples and exhibits the highest pseudocapacitive element Q3. The Warburg element is also at its lowest, suggesting that ion diffusion resistance is minimal despite the

higher dopant level. The increased V content introduces abundant redox-active sites, boosting faradaic storage, while still maintaining improved conductivity. However, the incremental benefit from 0.5% to 1% is relatively small; in some cases, excessively high dopant levels can slightly increase internal resistance or cause diminishing returns in capacitance gain. In this study, the SC5 device does not deliver the largest specific capacitance values but only marginally better impedance metrics than the 0.3% and 0.7% V-doped cells, indicating a saturation of the beneficial effects by 1% V. Minor experimental differences may give better dispersion of dopants. Although absolute values for the ZnS–V electrodes differ, the trend is similar: vanadium doping roughly doubles the low-rate capacitance from SC1 to SC5 (0% to 1% V) by introducing additional faradaic storage and enhancing conductivity.

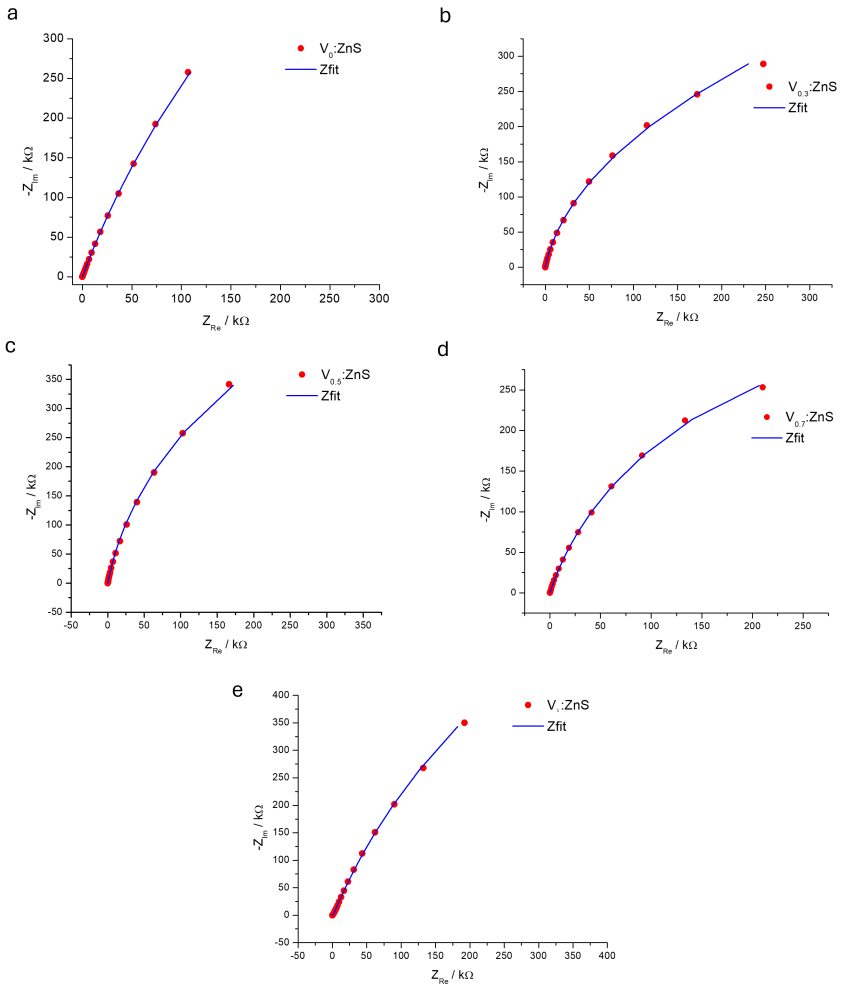

Figure 5.10 PEIS and Z-fit graphs of undoped ZnS (a), ZnS:V 0.3% (b), ZnS:V 0.5% (c), ZnS:V 0.7% (d), ZnS:V 1% (e).

Table 5.2 Equivalent circuit schematic and corresponding parameter values extracted from Nyquist plot fitting via Z-fit.

Sample	**R1** (Ω)	**R2** (Ω)	**R3** (Ω)	**Q2** ($\mathbf{F{\cdot}s^{\alpha-1}}$)	**Q3** ($\mathbf{F{\cdot}s^{\alpha-1}}$)	**W3** ($\Omega{\cdot}s^{-1/2}$)
SC1	0.607	2397	50.29	32.3	0.449	75.33
SC2	0.142	14	420	2.6	0.2205	52.72
SC3	0.481	12.13	133.9	28.9	44.8	5.05
SC4	0.274	25.94	766.24	5.05	24.96	14.7
SC5	0.164	21.79	13.97	21.95	50.67	22.83

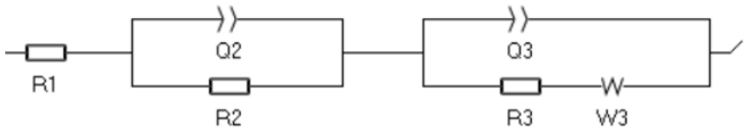

Figure 5.11 Equivalent circuit schematic.

5.6.3 Galvanostatic Charge–Discharge with Potential Limitation (GCPL)

GCPL graphs are instrumental in evaluating the electrochemical performance of materials used in SC devices. Fig 5.12 shows the specific capacity and GCPL graphs of undoped and vanadium-doped ZnS samples synthesized with varying dopant concentrations. V-doped ZnS samples generally display higher peak voltages compared to undoped ZnS, indicating enhanced charge storage capability and improved charge transfer kinetics. The GCPL curves for 0.5% and 0.7% V-doped ZnS samples exhibit more pronounced peak voltages with slightly sharper charge-discharge profiles, suggesting an optimal balance between electronic conductivity and structural stability at these doping levels. The deviation from purely capacitive to semi-diffusive behavior is further evidenced by the semi-triangular GCPL curves for higher doping levels, where Faradaic redox reactions contribute alongside the EDLC mechanism. In contrast, the 1% V-doped ZnS sample shows an earlier peak and rapid voltage decay, implying a possible defect-related limitations that hinder prolonged charge retention which is visible at Fig 5.13 for capacitive retention.

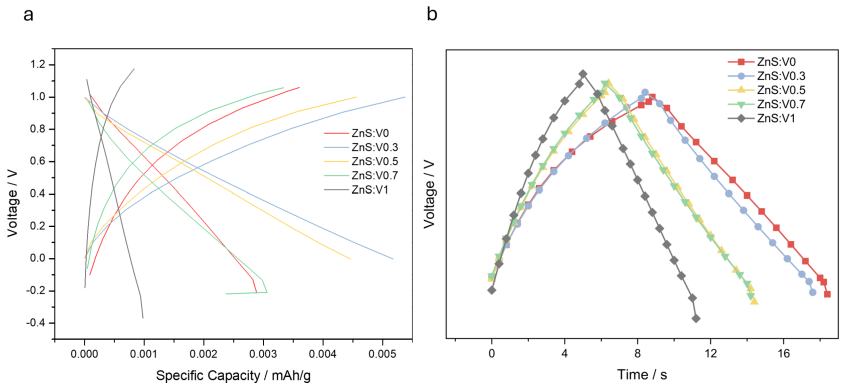

Figure 5.12 Specific capacity (a) and GCPL (b) plots of undoped and V-dopes ZnS samples.

Further insights are provided by the specific capacity profiles shown in Fig 5.12. The specific capacity curves indicate that ZnS:V 0.3% exhibits the highest capacity (~ 0.006 mAh/g) with close second ZnS:V 0.5%, while undoped ZnS shows relatively low capacity (~ 0.003 mAh/g). The capacity enhancement with V doping suggests improved active site utilization and better charge transfer, likely due to increased electronic conductivity and defect-induced redox activity. However, the specific capacity of the ZnS:V 1% sample is significantly lower than other doped samples, consistent with the rapid voltage decay observed in GCPL data. This indicates that excessive doping leads to structural or electronic limitations that reduce charge storage capability.

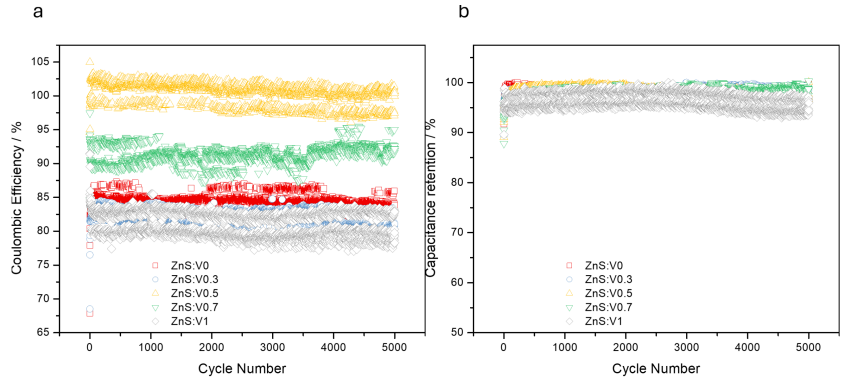

Figure 5.13 The Coulombic efficiency - CE (a) and the capacitive retention – CR (b) of the undoped and V-doped ZnS nanoparticles.

Several studies have demonstrated the effectiveness of ZnS incorporated nanostructures in enhancing the electrochemical performance of supercapacitors. For instance, Zhang *et al.* developed a nanoflower-structured $Zn_{0.76}Co_{0.24}S$ material directly grown on carbon fiber paper via a mild two-step hydrothermal method. When assembled into an all-solid-state asymmetric supercapacitor with activated carbon

as the negative electrode, the device achieved a maximum energy density of 9.59 Wh/kg at a power density of 750 W/kg (Zhang et al., 2019). Saleem et al. prepared zinc sulfide (ZnS) and a zinc sulfide/nickel oxide (ZnS/NiO) nanocomposite using a chemical coprecipitation technique. The ZnS/NiO symmetric supercapacitor achieved an energy density of 5.52Wh/kg and a power density of 1600W/kg when tested in a 1M KOH electrolyte solution (Saleem, Khalid, Nazir, Khan, & Farooq, 2024). Iqbal et al. fabricated a ZnS nanoweb directly on Ni foam that was pre-coated with a thin layer of graphene oxide synthesized via a hydrothermal method. The resulting GO-supported ZnS nanoweb exhibited an energy density of 20.29Wh/kg and a power density of 4407.73W/kg (Iqbal et al., 2018).

Fig 5.14 presents the Ragone plot for the SC devices, illustrating the maximum power density and energy density achieved by each device. The energy density (Ed) was determined using the Equation 4.6. The power density (P_d) was calculated by dividing the energy density (E_d) by the discharge time (Δt), which was obtained from the GCPL measurements for each device using Equation 5.1.

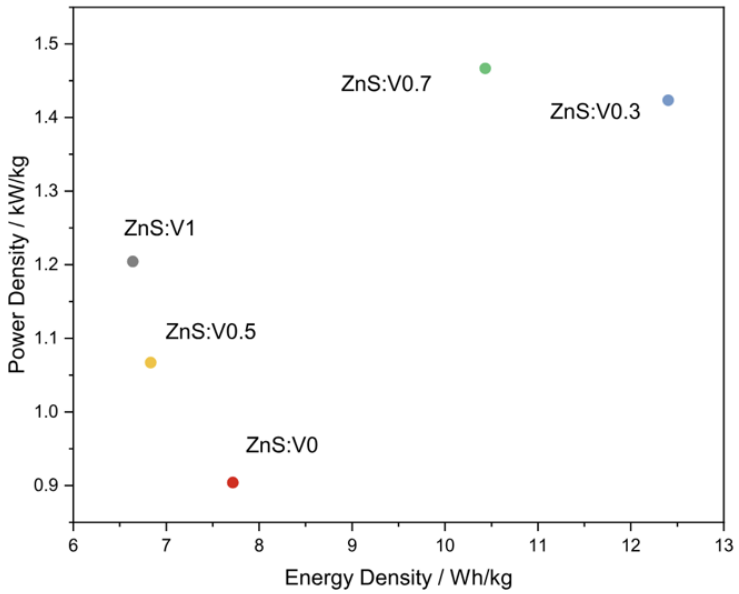

Figure 5.14 Ragone plot comparing the energy and power densities of the fabricated SC devices.

The ZnS:V 0.3% sample demonstrates the highest energy density among the tested electrodes, while ZnS:V 0.7% exhibits the greatest power density performance. Both ZnS:V 1% and ZnS:V 0.5% samples also show improved power density compared to undoped ZnS. The enhanced electrochemical performance observed in the vanadium-doped samples can be attributed to multiple factors. Incorporation of vanadium ions into the ZnS lattice introduces additional charge carriers, thereby facilitating

more efficient ion diffusion and enhancing Faradaic redox reaction kinetics within the system. However, while vanadium doping generally provides an optimal balance between increasing charge carriers and maintaining structural integrity, excessive dopant incorporation, as seen in the ZnS:V 1% sample, may adversely affect conductivity or induce higher recombination losses, ultimately limiting its overall performance.

In summary, the findings indicate that moderate levels of vanadium doping, specifically within the 0.3–0.7% range, significantly enhance the electrochemical performance of ZnS-based supercapacitor devices by simultaneously increasing conductivity and specific capacitance while maintaining structural stability. Comparable observations have been reported in other studies involving transition metal-doped sulfide and oxide materials, where carefully optimized doping concentrations were shown to improve electrochemical kinetics and preserve capacitive performance over prolonged cycling.

6. CONCLUSION

This study has comprehensively explored the structural, optical, and electrochemical impacts of V doping on ZnS nanoparticles synthesized via precipitation synthesis, with a particular emphasis on their applicability as electrode materials in supercapacitors. The findings substantiate the hypothesis that vanadium incorporation significantly enhances the charge storage capabilities of ZnS, primarily through defect engineering and modulation of electronic structure.

XRD confirmed that all synthesized samples maintained a sphalerite cubic structure, with subtle lattice distortions induced by vanadium substitution. These structural shifts were corroborated by changes in crystallite size and unit cell volume, consistent with the larger ionic radius of V^{+2} compared to Zn^{+2}. The increase in crystallite size and lattice parameters at moderate doping levels suggests successful substitutional doping rather than mere surface adsorption, which is a critical factor in modulating the bulk properties of the host lattice.

UV–Vis absorption studies revealed a modulation of the optical bandgap with increasing vanadium concentration, first showing a decrease due to sp–d exchange interactions, followed by a slight increase explained by the Burstein–Moss effect. These changes indicate that vanadium doping not only introduces localized defect levels but also alters the carrier concentration and electronic transitions in the material. Scanning transmission electron microscopy (STEM) images supported these interpretations by showing uniform particle dispersion with spherical morphology, further confirmed by elemental mapping.

EPR spectroscopy provided direct evidence of paramagnetic centers and hyperfine splitting due to V^{+4} ions, validating the presence of isolated and interacting vanadium dopants. The spectra confirmed the formation of defect structures and demonstrated their critical role in enabling redox-active behavior within the ZnS lattice. Complementarily, PL spectroscopy revealed emissions linked to intrinsic and extrinsic defect states. The presence of blue and green emissions, along with doping-induced orange-red emissions, underscored the formation defect centers, enhancing

pseudocapacitive contributions.

Electrochemical characterizations through CV, PEIS, and GCPL established the performance advantages of vanadium doping. CV profiles of V-doped ZnS samples demonstrated greater current response, redox activity, and charge storage capacity, particularly at 0.3%, 0.5%, and 0.7% doping levels. Dunn analysis quantitatively distinguished the balance between capacitive and diffusive contributions, showing that vanadium doping enhances pseudocapacitive behavior, mainly through Faradaic processes facilitated by multivalent redox transitions ($V^{+3}/V^{+4}/V^{+5}$). The capacitive contributions diminished beyond 0.7% doping, suggesting saturation or adverse structural effects at higher doping levels.

PEIS measurements further supported these findings by showing a marked decrease in charge transfer resistance and Warburg impedance in V-doped samples. Notably, the ZnS:V 0.5% and 0.7% samples exhibited the most favorable impedance characteristics, indicating fast ion transport and low internal resistance. The presence of well-distributed defect states and enhanced electrical conductivity, as inferred from the increased Q3 values, contributed significantly to their superior performance.

GCPL analysis revealed that V-doped ZnS electrodes demonstrated higher specific capacity, better Coulombic efficiency, and more stable charge–discharge profiles compared to undoped samples. The Ragone plots indicated a simultaneous enhancement in both energy and power densities for V-doped samples, with ZnS:V 0.3% achieving the highest energy density and ZnS:V 0.7% delivering the highest power density. However, at 1% V doping, a decline in electrochemical performance was observed, likely due to structural instabilities, defect saturation, or dopant agglomeration.

In conclusion, this work confirms that controlled vanadium doping is a promising strategy for enhancing the electrochemical performance of ZnS electrodes. Integrating the spectroscopic and electrochemical findings provides a clear picture of how vanadium induced defects influence charge storage in ZnS. EPR confirms that vanadium substitutes into the ZnS lattice as V^{+4}, creating paramagnetic centers. The multivalence of vanadium ($V^{+3}/V^{+4}/V^{+5}$) allows these dopant centers to undergo fast, reversible redox transitions, directly contributing to pseudocapacitance. This is evidenced by Dunn analysis of the CV data, which shows a significantly larger diffusion-controlled charge contribution in V-doped ZnS compared to undoped ZnS. PL spectroscopy further reveals that new mid-gap defect levels are introduced upon doping, as indicated by the appearance of additional emission bands in the doped samples. In practice, such defect sites facilitate extra Faradaic reactions beyond the electric double-layer mechanism, enabling ions and electrons to interact more effectively and thus boosting the overall capacitance and energy storage of the material.

In addition to providing these redox-active sites, vanadium doping also improves the charge transport kinetics of ZnS. Consistently, PEIS results show that moderately doped samples (0.5–0.7% V) have a markedly lower charge-transfer resistance and reduced Warburg impedance than undoped ZnS, indicating faster electron transport and ion diffusion in the presence of V-induced defects. This improvement in conductivity translates into better charge-discharge performance. GCPL confirms that V-doped ZnS electrodes deliver higher specific capacities and sustain more efficient cycling than the undoped material. At the highest dopant concentration (1% V), however, the benefits of defect engineering are reversed. Such excessive doping likely introduces lattice strain or agglomerated dopants that outweigh the advantages of additional redox sites, as reflected in the electrochemical measurements: beyond $\sim 0.7\%$ vanadium content the internal resistance rises and ion diffusion is hindered, leading to a drop in capacitance. Consequently, there exists an optimal defect concentration for maximizing performance which around 0.3–0.7% V, beyond which further doping degrades the charge storage efficiency of the ZnS electrode.

Future investigations should prioritize the systematic optimization of the defect chemistry in ZnS through the implementation of advanced doping strategies. In particular, co-doping with multiple transition metals, such as nickel, iron, or manganese could introduce synergistic effects that significantly enhance the redox activity, electrical conductivity, and ionic mobility within the electrode material. Such multielemental doping approaches may also facilitate the formation of additional defect sites and modify the electronic structure of ZnS, thereby improving its electrochemical performance. Furthermore, engineering ZnS nanostructures beyond conventional spherical morphologies, such as developing nanosheets, nanowires, hollow architectures, or hierarchical porous frameworks can play a critical role in promoting faster ion diffusion and maximizing the exposure of electrochemically active sites. These structural innovations, when combined with optimized compositional tuning, may contribute to the development of next-generation ZnS-based materials with better energy storage capabilities.

BIBLIOGRAPHY

Adachi, S. (1999). Cubic zinc sulphide (β-zns). In *Optical constants of crystalline and amorphous semiconductors: Numerical data and graphical information* (pp. 445–458). Springer.

Adams, F., & Barbante, C. (2015). Spectroscopic imaging. In *Comprehensive analytical chemistry* (Vol. 69, pp. 339–384). Elsevier.

Ahmad, S. A., Arif, M., Hussain, I., Liu, Y., Zhang, W., & Zhu, T. (2025). Integrating zns microspheres with bi2se3 sponge ball structures to realize high energy density with good stability for supercapacitors. *APL Materials*, *13*(5).

Ahmed, M. M. S., Hasan, M. J., Chowdhury, M. S., Rahman, M. K., Islam, M. S., Hossain, M. S., ... Mobarak, M. H. (2024). Prospects and challenges of energy storage materials: a comprehensive review. *Chemical Engineering Journal Advances*, *20*, 100657.

Alam, S., Khan, Q. Z., Gassoumi, A., Khan, M. I., Iqbal, M. Z., & Ahmad, Z. (2024). Innovating synthesis approaches in advancing electrochemical efficiency: A journey into hydrothermal and sonochemical realms. *Journal of Energy Storage*, *78*, 109821.

An, Q., Meng, X., Xiong, K., & Qiu, Y. (2017). Self-powered zns nanotubes/ag nanowires msm uv photodetector with high on/off ratio and fast response speed. *Scientific reports*, *7*(1), 4885.

Ardelean, I., Cozar, O., Vedeanu, N., Rusu, D., & Andronache, C. (2007). Epr study of v2o5–p2o5–li2o glass system. *Journal of Materials Science: Materials in Electronics*, *18*(9), 963–966.

Azizpour, A., Bagovic, N., Ploumis, N., Mylonas, K., Hoxha, D., Kienberger, F., ... Gramse, G. (2025). Electrochemical analysis of carbon-based supercapacitors using finite element modeling and impedance spectroscopy. *Energies*, *18*(6), 1450.

Baumann, S., Paul, W., Choi, T., Lutz, C. P., Ardavan, A., & Heinrich, A. J. (2015). Electron paramagnetic resonance of individual atoms on a surface. *Science*, *350*(6259), 417–420.

Choi, W., Shin, H.-C., Kim, J. M., Choi, J.-Y., & Yoon, W.-S. (2020). Modeling and applications of electrochemical impedance spectroscopy (eis) for lithium-ion batteries. *Journal of Electrochemical Science and Technology*, *11*(1), 1–13.

Dissanayake, K., & Kularatna-Abeywardana, D. (2024). A review of supercapacitors: Materials, technology, challenges, and renewable energy applications. *Journal of Energy Storage*, *96*, 112563.

Dong, Q., Li, S., Liu, R., Liu, B., Li, Q., Kim, J., & Liu, B. (2022). A morphology-dependent lattice stability investigation in zns nanostructures by high-pressure xafs studies. *Journal of Materials Chemistry C*, *10*(33), 11959–11966.

D'Amico, P., Calzolari, A., Ruini, A., & Catellani, A. (2017). New energy with zns: novel applications for a standard transparent compound. *Scientific reports*, *7*(1), 16805.

El Khouja, O., Boukhoubza, I., Derkaoui, I., Assahsahi, I., Achehboune, M., Talbi, A., ... Nouneh, K. (2024). Investigation of structural and optical properties of mg doped zns thin films prepared by mist-cvd technique: Experimental and

theoretical aspects. *Materials Chemistry and Physics*, *313*, 128707.

Erbe, A., Nayak, S., Chen, Y.-H., Niu, F., Pander, M., Tecklenburg, S., & Toparli, C. (2018). How to probe structure, kinetics, and dynamics at complex interfaces in situ and operando by optical spectroscopy. *Encyclopedia of interfacial chemistry*, 199–219.

Fick, J. (2001). Crystalline nanoparticles in glasses for optical applications. In *Handbook of surfaces and interfaces of materials* (pp. 311–350). Elsevier.

Forouzandeh, P., Kumaravel, V., & Pillai, S. C. (2020). Electrode materials for supercapacitors: a review of recent advances. *Catalysts*, *10*(9), 969.

Gahlot, P., Agarwal, A., Seth, V., Sanghi, S., Gupta, S., & Arora, M. (2005). Study of epr, optical properties and electrical conductivity of vanadyl doped bi2o3 · pbo · b2o3 glasses. *Spectrochimica Acta Part A: Molecular and Biomolecular Spectroscopy*, *61*(6), 1189–1194.

Ganguly, S., Halder, K., Haque, N. A., Das, S., & Dastidar, S. (2015). A comparative study between electrical properties of bulk and synthesized nano material of zinc sulphide. *American Journal of Research Communication*, *3*(3), 1–13.

Guo, J., Zhao, H., Yang, Z., Wang, L., Wang, A., Zhang, J., ... Yu, X. (2024). Bimetallic sulfides with vacancy modulation exhibit enhanced electrochemical performance. *Advanced Functional Materials*, *34*(28), 2315714.

Haque, F., Rahman, K., Islam, M., Rashid, M., Akhtaruzzaman, M., Alam, M., ... Amin, N. (2014). Growth optimization of zns thin films by rf magnetron sputtering as prospective buffer layer in thin film solar cells. *Chalcogenide Lett*, *11*(4), 189–197.

Hroub, A., Aleinawi, M. H., Stefan, M., Mihet, M., Ciorita, A., Bakan-Misirlioglu, F., ... Rostas, A. M. (2023). Vanadium-doped magnesium oxide nanoparticles as electrodes in supercapacitor devices. *Journal of Alloys and Compounds*, *958*, 170442.

Huang, J. (2018). Diffusion impedance of electroactive materials, electrolytic solutions and porous electrodes: Warburg impedance and beyond. *Electrochimica Acta*, *281*, 170–188.

Iqbal, M. F., Razaq, A., Ashiq, M. N., Kaneti, Y. V., Azhar, A. A., Yasmeen, F., ... Abbass, S. (2018). Effect of graphene oxide thin film on growth and electrochemical performance of hierarchical zinc sulfide nanoweb for supercapacitor applications. *ChemElectroChem*, *5*(18), 2636–2644.

Jakes, P., & Erdem, E. (2011). Finite size effects in zno nanoparticles: An electron paramagnetic resonance (epr) analysis. *physica status solidi (RRL)–Rapid Research Letters*, *5*(2), 56–58.

Jubeer, E. M., Manthrammel, M. A., Subha, P., Shkir, M., Biju, K., & AlFaify, S. (2023). Defect engineering for enhanced optical and photocatalytic properties of zns nanoparticles synthesized by hydrothermal method. *Scientific Reports*, *13*(1), 16820.

Kar, S., & Chaudhuri, S. (2005). Controlled synthesis and photoluminescence properties of zns nanowires and nanoribbons. *The Journal of Physical Chemistry B*, *109*(8), 3298–3302.

Lazanas, A. C., & Prodromidis, M. I. (2023). Electrochemical impedance spectroscopy a tutorial. *ACS measurement science au*, *3*(3), 162–193.

Lee, G.-J., Anandan, S., Masten, S. J., & Wu, J. J. (2014). Sonochemical synthesis of hollow copper doped zinc sulfide nanostructures: optical and catalytic

properties for visible light assisted photosplitting of water. *Industrial & Engineering Chemistry Research*, *53*(21), 8766–8772.

Lee, S., Song, D., Kim, D., Lee, J., Kim, S., Park, I. Y., & Choi, Y. D. (2004). Effects of synthesis temperature on particle size/shape and photoluminescence characteristics of zns: Cu nanocrystals. *Materials Letters*, *58*(3-4), 342–346.

Li, X., Cao, J., Yang, L., Wei, M., Liu, X., Liu, Q., ... Yang, J. (2019). One-pot synthesis of zns nanowires/cu 7 s 4 nanoparticles/reduced graphene oxide nanocomposites for supercapacitor and photocatalysis applications. *Dalton Transactions*, *48*(7), 2442–2454.

Lindon, J. C., Tranter, G. E., & Koppenaal, D. (2016). *Encyclopedia of spectroscopy and spectrometry*. Academic Press.

Liu, H., Hu, L., Watanabe, K., Hu, X., Dierre, B., Kim, B., ... Fang, X. (2013). Cathodoluminescence modulation of zns nanostructures by morphology, doping, and temperature. *Advanced Functional Materials*, *23*(29), 3701–3709.

Liu, J., Zhang, J.-G., Yang, Z., Lemmon, J. P., Imhoff, C., Graff, G. L., ... others (2013). Materials science and materials chemistry for large scale electrochemical energy storage: from transportation to electrical grid. *Advanced Functional Materials*, *23*(8), 929–946.

Mane, S. M., Wagh, K. S., Teli, A. M., Beknalkar, S. A., Shin, J. C., & Lee, J. (2024). One-pot facile synthesis of a cluster of zns low-dimensional nanoparticles for high-performance supercapacitor electrodes. *Micromachines*, *15*(2), 251.

Maswanganye, M. W., Kabongo, G. L., & Dhlamini, M. S. (2022). Modulating charge mobility in microwave synthesized ti-doped zns nanoparticles for potential photoanode applications. *Nanomaterials*, *13*(1), 77.

Mehra, P., Saxena, S., & Bhullar, S. (2024). A comprehensive analysis of supercapacitors and their equivalent circuits—a review. *World Electric Vehicle Journal*, *15*(8), 332.

Mitrić, J. (2022). Properties and characterization of rare-earth-activated phosphors. In *Rare-earth-activated phosphors* (pp. 43–58). Elsevier.

Owens, F. J. (2005). Ferromagnetism above room temperature in bulk sintered gallium phosphide doped with manganese. *Journal of Physics and Chemistry of Solids*, *66*(5), 793–796.

Panchu, S. J., Raju, K., & Swart, H. C. (2024). Emerging two–dimensional intercalation pseudocapacitive electrodes for supercapacitors. *ChemElectroChem*, *11*(15), e202300810.

Parashar, S., Murty, B., Repp, S., Weber, S., & Erdem, E. (2012). Investigation of intrinsic defects in core-shell structured zno nanocrystals. *Journal of Applied Physics*, *111*(11).

Rana, M. S., Das, S. K., Rahman, M. O., Ahmed, F., & Hossain, M. A. (2021). Vanadium doped zns nanoparticles: effect of vanadium concentration on structural, optical and electrical properties. *Transactions on Electrical and Electronic Materials*, *22*(5), 612–621.

Rathore, K. S., Patidar, D., Janu, Y., Saxena, N., Sharma, K., & Sharma, T. (2008). Structural and optical characterization of chemically synthesized zns nanoparticles. *Chalcogenide Lett*, *5*(6), 105–110.

Reddy, A. J., Kokila, M., Nagabhushana, H., Rao, J., Shivakumara, C., Nagabhushana, B., & Chakradhar, R. (2011). Epr, thermo and photoluminescence properties of zno nanopowders. *Spectrochimica Acta Part A: Molecular and*

Biomolecular Spectroscopy, *81*(1), 59–63.

Saleem, S., Khalid, S., Malik, M. A., & Nazir, A. (2024). Review and outlook of zinc sulfide nanostructures for supercapacitors. *Energy & Fuels*, *38*(11), 9153–9185.

Saleem, S., Khalid, S., Nazir, A., Khan, Y., & Farooq, K. (2024). Electrochemical investigation of zns/nio nanocomposite based symmetric supercapattery. *ChemistrySelect*, *9*(25), e202400809.

Shah, M. Z. U., Sajjad, M., Hou, H., BiBi, S., & Shah, A. (2022). Hydrothermal synthesis of zno@ zns heterostructure on ni foam: A binder free electrode for high power and stable hybrid supercapacitors. *Materials Letters*, *326*, 132910.

Shreya, Phogat, P., Jha, R., & Singh, S. (2023). Microwave-synthesized γ-wo3 nanorods exhibiting high current density and diffusion characteristics. *Transition Metal Chemistry*, *48*(3), 167–183.

Shrivastav, V., Sundriyal, S., Goel, P., Saha, A., Tiwari, U. K., & Deep, A. (2021). A novel zinc sulfide impregnated carbon composite derived from zeolitic imidazolate framework-8 for sodium-ion hybrid solid-state flexible capacitors. *Nanoscale Advances*, *3*(21), 6164–6175.

Shukla, U., & Bari, S. (2018). Study on the photoluminescence. *Journal of Pure Applied and Industrial Physics*, *8*(5), 25–31.

Stefan, M., Toloman, D., Popa, A., Mesaros, A., Vasile, O., Leostean, C., & Pana, O. (2016). Interface charge transfer process in zno: Mn/zns nanocomposites. *Journal of Nanoparticle Research*, *18*(3), 59.

Tom, E., Velluva, A., Joseph, A., Thomas, T., Sha, M. S., Jithin, P., ... Kurian, J. (2025). Tailoring the electrochemical properties of zns electrodes via cobalt doping for improved supercapacitor application. *Journal of Electronic Materials*, *54*(1), 451–461.

Vivier, V., & Orazem, M. E. (2022). Impedance analysis of electrochemical systems. *Chemical Reviews*, *122*(12), 11131–11168.

Wright, A. C., & Viney, I. V. (2001). A structural evaluation of zns-based electroluminescent phosphors and devices: a comparison with performance. *Philosophical Magazine B*, *81*(3), 279–297.

Xiao, N., Dai, Q., Wang, Y., Ning, J., Liu, B., Zou, G., & Zou, B. (2012). Zns nanocrystals and nanoflowers synthesized by a green chemistry approach: Rare excitonic photoluminescence achieved by the tunable molar ratio of precursors. *Journal of hazardous materials*, *211*, 62–67.

Yadlapalli, R. T., Alla, R. R., Kandipati, R., & Kotapati, A. (2022). Super capacitors for energy storage: Progress, applications and challenges. *Journal of Energy Storage*, *49*, 104194.

Yamada, H., Yoshii, K., Asahi, M., Chiku, M., & Kitazumi, Y. (2022). Cyclic voltammetry part 1: fundamentals. *Electrochemistry*, *90*(10), 102005–102005.

Yi, T.-F., Li, Y., Li, Y.-M., Luo, S., & Liu, Y.-G. (2019). Zns nanoparticles as the electrode materials for high-performance supercapacitors. *Solid State Ionics*, *343*, 115074.

Zhang, M., Sui, Y., Yuan, X., Qi, J., Wei, F., Meng, Q., ... Liu, J. (2019). Controllable zn 0. 7 6 co 0. 2 4 s nanoflower arrays grown on carbon fiber papers for high-performance supercapacitors. *Nano*, *14*(03), 1950030.

Zhu, M., Wang, D., Ge, Z., Pan, L., Chen, Y., Wang, W., ... Chen, Z. (2025). Recent advances in transition metal sulfide-based electrode materials for su-

percapacitors. *Chemical Communications*, *61*(46), 8314–8326.